

High energy particles from young supernovae: gamma-ray and neutrino connections

Prantik Sarmah,^a Sovan Chakraborty,^a Irene Tamborra,^b and Katie Auchettl^{c,d,e}

^aDepartment of Physics, Indian Institute of Technology Guwahati, Guwahati, Assam-781039, India

^bNiels Bohr International Academy and DARK, Niels Bohr Institute, University of Copenhagen, Blegdamsvej 17, 2100, Copenhagen, Denmark

^cSchool of Physics, The University of Melbourne, Parkville, VIC 3010, Australia

^dARC Centre of Excellence for All Sky Astrophysics in 3 Dimensions (ASTRO 3D)

^eDepartment of Astronomy and Astrophysics, University of California, Santa Cruz, CA 95064, USA

E-mail: prantik@iitg.ac.in, sovan@iitg.ac.in, tamborra@nbi.ku.dk, katie.auchettl@unimelb.edu.au

Abstract. Young core-collapse supernovae (YSNe) are factories of high-energy neutrinos and gamma-rays as the shock accelerated protons efficiently interact with the protons in the dense circumstellar medium. We explore the detection prospects of secondary particles from YSNe of Type IIn, II-P, IIb/II-L, and Ib/c. Type IIn YSNe are found to produce the largest flux of neutrinos and gamma-rays, followed by II-P YSNe. Fermi-LAT and the Cherenkov Telescope Array (IceCube-Gen2) have the potential to detect Type IIn YSNe up to 10 Mpc (4 Mpc), with the remaining YSNe Types being detectable closer to Earth. We also find that YSNe may dominate the diffuse neutrino background, especially between 10 TeV and 10^3 TeV, while they do not constitute a dominant component to the isotropic gamma-ray background observed by Fermi-LAT. At the same time, the IceCube high-energy starting events and Fermi-LAT data already allow us to exclude a large fraction of the model parameter space of YSNe otherwise inferred from multi-wavelength electromagnetic observations of these transients.

Contents

1	Introduction	1
2	Neutrino and gamma-ray production in young supernovae	3
2.1	Model setup	3
2.2	Gamma-ray production	5
2.3	Neutrino production	7
3	Young supernova types	8
4	Dependence of the gamma-ray and neutrino emission on the young supernova type	10
4.1	Characteristic gamma-ray and neutrino emission	11
4.2	Dependence on the young supernova type	13
5	Diffuse gamma-ray and neutrino backgrounds from young supernovae	15
5.1	Diffuse flux and its ingredients	15
5.2	Diffuse background of gamma-rays	17
5.3	Diffuse background of high-energy neutrinos	18
5.4	Model parameter uncertainties	19
5.5	Discussion	20
6	Detection prospects of nearby young supernovae in gamma-rays and neutrinos	23
7	Conclusions	24
A	Characteristic timescales for proton acceleration and radiative processes	26

1 Introduction

The IceCube Neutrino Observatory routinely detects high-energy neutrinos of astrophysical origin, whose origin remains unknown [1–4]. Various source classes have been proposed to explain the IceCube neutrino flux [5–8], such as galaxy clusters, (low-luminosity or choked) gamma-ray bursts, tidal disruption events, star-forming galaxies, and supernovae (SNe) [9–21]. However, none of these sources can fully explain the IceCube data, hinting that more than one source class contributes to the overall observed flux [22, 23]. In addition to the diffuse background of high-energy neutrinos, neutrino events have been observed in likely associations with blazars [24–29], tidal disruption events [30, 31], and a hydrogen-rich superluminous SN [32]. Moreover, ongoing electromagnetic follow-up searches, see e.g. [27, 33, 34], promise to provide key insight to disentangle the origin of the ever growing number of IceCube neutrino events of astrophysical origin.

The high-energy neutrino events observed by the IceCube Neutrino Observatory are believed to have a correspondent counterpart in gamma-rays possibly observable by Fermi-LAT, see e.g. [13, 28, 35–43]. This is because such high energy particles originate from

the decay of charged and neutral pions produced in hadronic interactions such as proton-proton (pp) collisions or photo-hadronic ($p\gamma$) interactions [44, 45]. In this respect special attention has been devoted to the possible common origin of the IceCube diffuse flux of high-energy neutrinos [46] and the extragalactic diffuse gamma-ray background observed by Fermi-LAT [47]. Evidence suggests that the latter originates from the superposition of unresolved extragalactic sources, such as blazars, star-forming galaxies, gamma-ray bursts, etc. [13, 47–59].

Supernovae constitute a particularly interesting source class, possibly emitting high-energy neutrinos and gamma-rays through inelastic pp collisions between the relativistic protons accelerated at the SN shock and the low energy protons of the circumstellar medium (CSM) [60–66]. In fact, the existence of dense CSM around massive stars has been confirmed by multi-wavelength observations of a wide range of phenomena, e.g., [67, 68]. The CSM is made up of matter deposited through stellar winds further enriched as the progenitor star loses mass via wind and/or violent outbursts (e.g., see Ref. [67] and references therein). The CSM was previously thought to originate from stars losing their mass through steady stellar winds. However, recent SN observations have challenged this traditionally accepted picture (see e.g. [67]). It is now clear that substantial and impulsive mass losses occur in at least 10% of massive stars within one year from the core collapse.

The stellar progenitor of SN2009ip, whose repeated eruptions occurred in the years before explosion, is the best studied example among Hydrogen (H)-rich massive stars [69]. The progenitor of this SN was a Luminous Blue Variable (LBV) star. An LBV is a massive star that can have sporadic, violent mass loss events and exhibits mass loss rate as high as $10 M_{\odot}\text{yr}^{-1}$ [70–73]. LBVs were previously thought to be a transitional phase of stellar evolution. However, several recent works have shown that they can be progenitors of Type IIIn SNe (see e.g. [74] and references therein). The interaction between the CSM and the SN ejecta is evident from the observation of narrow, symmetric emission lines in “flash” spectroscopy of SNe. This might be due to the photo-ionization of the CSM occurring during the progenitor mass loss phase before explosion, see e.g. [75, 76]. UV/optical excesses observed in SNe at early times also hint towards such mass loss phenomena, see e.g. [77].

In most cases, the interaction of the SN shock with the CSM is dominant during the early stages of the SN evolution, for a few months to a few years [78]. After this preliminary phase, the interaction weakens due to the fall in the CSM density [79]. We focus on the high-energy particle emission during this initial SN phase and refer to it as “Young Supernova (YSN)”. Note that, a clear distinction between YSNe and SN remnants (SNRs) is not straightforward [64, 80, 81]. In a SNR, the SN ejecta interacts with and sweeps up the far away CSM or the Interstellar Medium (ISM). For a sufficiently old SNR (1 kyr), the medium is significantly less dense and has a density of $1 - 10^3 \text{ cm}^{-3}$. While the dense CSM during the YSN phase can have densities in the scale of $10^9 - 10^{12} \text{ cm}^{-3}$ [19, 59, 82, 83]. Thus the largest contribution to the secondary particle emission is reasonably considered to originate from the YSN phase.

The high-energy neutrinos emitted from SNe are possibly detectable by the IceCube Neutrino Observatory [19, 39, 63, 84]. In addition, gamma-rays could be observed from SNe by Fermi-LAT [47, 50, 85] and the Cerenkov Telescope Array (CTA) [86]. Recently, Fermi-LAT detected gamma-rays from the direction of a peculiar supernova iPTF14hls [87]. Such discovery is however uncertain because of the presence of a blazar in the detection error circle.

Varying mass and metallicity of stars may give rise to different SN Types [88, 89]. By considering YSNe of Type IIIn, II-P, II-L and Ib/c, we explore the related gamma-ray and

neutrino emission and investigate their detection prospects with Fermi-LAT [47, 85] and CTA [86] as well as IceCube [3, 90], IceCube-Gen2 [91], and Km3NeT [92].

While neutrinos produced in YSNe propagate undisturbed to Earth, gamma-rays undergo energy losses as they interact with low energy photons ($\gamma\gamma \rightarrow e^-e^+$) and ambient matter ($\gamma N \rightarrow Ne^-e^+$, where N is nucleus) in the source [93]. In addition, over cosmic scales ($\sim \text{Gpc}$), the Extra-galactic Background Light (EBL) absorption further affects the gamma-ray flux expected at Earth [52, 94], becoming significant for the diffuse SN emission, but negligible for point source detection in the local universe (i.e., below $\sim 10 \text{ Mpc}$).

This paper is organized as follows. In Sec. 2, we introduce our YSN model with interacting CSM and the related production of secondary particles: neutrinos and gamma-rays. Different Types of YSNe and their properties are discussed in Sec. 3. The dependence of the gamma-ray and neutrino emission on the YSN Types is explored in Sec. 4. The diffuse gamma-ray and neutrino backgrounds from YSNe are presented in Sec. 5 together with a discussion on the model parameter uncertainties and the detection prospects. The detection prospects of YSNe in the local universe with present and upcoming gamma-ray and neutrino telescopes are analysed in Sec. 6. Finally, we summarize our findings in Sec. 7. An overview on the characteristic time scales for particle acceleration and energy losses of protons is provided in Appendix A.

2 Neutrino and gamma-ray production in young supernovae

In this Section, we model YSNe interacting with the CSM in the early phase after the explosion. We focus on YSNe about a year old and develop a model for the shock-CSM interaction, describing the creation of secondary particles: neutrinos and anti-neutrinos ¹ and gamma-rays.

2.1 Model setup

The material expelled by the massive star at the end of its life forms the CSM. The CSM consists of shells of mostly light elements like H or helium (He). The massive star eventually explodes in the form of a core-collapse SN ². The SN shock and the expanding ejecta interact with the surrounding CSM. Charged particles (electrons and protons) in the shocked CSM are accelerated to relativistic energies via Fermi’s diffusive shock acceleration [96–98]. In particular, we are interested in high energy processes with dominant neutrino production, hence we focus on inelastic pp collisions. Here, relativistic protons collide with the non-relativistic protons (inelastic pp collisions) in the CSM and produce a large number of π and η mesons. Secondary neutrinos, electrons and gamma-rays are produced from the decay of π and η mesons [19, 44, 83, 99–101]. High energy protons can also undergo photo-hadronic ($p\gamma$) interactions with low energy photons in the CSM. However, the energy loss due to this process is negligible and hence neglected (see Appendix 7).

The CSM shell is assumed to be spherically symmetric with an effective inner radius r_{in} and outer radius r_{out} . The inner radius is defined as $r_{\text{in}} = \max[r_{\text{bo}}, r_e]$ [84]. The shock breakout radius³, r_{bo} , corresponds to the beginning of shock acceleration, and r_e is the radius

¹Note that we do not distinguish between particles and antiparticles in the following and use “neutrinos” to indicate both species.

²We focus on core-collapse SNe as the vast majority of Type Ia SNe do not exhibit a dense CSM (with the notable exception of e.g., [95]).

³The shock breakout radius corresponds to the optical depth, $\tau = c/v_{\text{sh}}$, of the material through which the shock propagates, where v_{sh} is the shock velocity introduced in the following [102].

of the stellar envelope. Thus r_{in} may differ according to the SN Type (see Sec. 3 for details). The outer radius or size of the CSM shell also depends on the SN Type. Given the assumption of spherical symmetry, the radial dependence of the CSM mass density can be modelled in the following way [64]:

$$\rho_{\text{CSM}}(r) = \frac{\dot{M}_{\text{W}}}{4\pi r_{\text{in}}^w v_{\text{w}}} \left(\frac{r_{\text{in}}}{r} \right)^w. \quad (2.1)$$

Here w is the power-law index of the CSM density profile (e.g., $w = 2$ for a wind-like CSM—see, e.g., Ref. [78]), \dot{M}_{W} is the mass loss rate of the progenitor star and v_{w} is the wind velocity. The radial dependence is provided by the propagation of the shock, r being the shock radius. The number density of the protons in the CSM ($n_{\text{CSM}}(r) = \rho_{\text{CSM}}(r)/m_{\text{p}}$) also varies accordingly. Thus, the CSM at the inner radius is $n_{\text{in,CSM}} = \rho_{\text{CSM}}(r_{\text{in}})/m_{\text{p}} = \dot{M}_{\text{W}}/(4\pi m_{\text{p}} r_{\text{in}}^2 v_{\text{w}})$, where m_{p} is the mass of the proton.

A fraction of the protons injected in the shocked region will be accelerated to high energies and in turn produce secondary particles while interacting with the CSM protons. To model this, the SN shock is assumed to expand spherically in the CSM and has a power law dependence on the radius. The velocity of the shock (v_{sh}) expanding in the CSM varies slowly with radius [78]:

$$v_{\text{sh}}(r) = v_{\text{in}} \left(\frac{r}{r_{\text{in}}} \right)^{\alpha}, \quad (2.2)$$

where v_{in} is the shock velocity at r_{in} and α characterises the shock velocity profile. The index α can be expressed in terms of the power law indices of the CSM and SN ejecta density profiles and is usually found to be negligible, i.e. the shock velocity is nearly constant over the length of the CSM shell during the early phase of the YSN. For more details on the choice of α , see Ref. [101]. In our YSN computations, we assume $\alpha = 0$ implying $v_{\text{sh}} = v_{\text{in}}$.

To estimate the secondary particle population, we need the injection spectra of the accelerated protons in the shocked region. We assume a power law distribution between the maximum ($E_{\text{p,max}}$) and minimum ($E_{\text{p,min}}$) proton energy for the injection spectra [83]:

$$N_{\text{p}}^{\text{inj}}(E_{\text{p}}, r) \propto E_{\text{p}}^{-\alpha_{\text{p}}} \exp \left(-\frac{E_{\text{p}}}{E_{\text{p,max}}(r)} \right), \quad (2.3)$$

where E_{p} is the proton energy, α_{p} is the power law index and it is assumed to be equal to 2 unless otherwise mentioned. The choice $\alpha_{\text{p}} = 2$ is motivated by diffusive shock acceleration theory [98]. The normalization of the injected spectra is obtained from the energy budget of the shock [$E_{\text{K}} = (9\pi/8)m_{\text{p}}v_{\text{sh}}^2 r^2 n_{\text{CSM}}(r)$, energy per unit radius]. A fraction of this energy, ϵ_{p} , is transferred to the charged particles (protons) confined in the shocked region due to the presence of a strong magnetic field and thus accelerates protons to high energies. The fraction ϵ_{p} is a free parameter of the problem and may depend on the SN Type. This is due to the fact that CSM density, ejecta kinetic energy and progenitor mass vary for different SN Types [103]. The minimum proton energy $E_{\text{p,min}}$ is taken as the proton rest mass m_{p} . The maximum energy ($E_{\text{p,max}}$) of the accelerated protons depends on the different loss processes competing with the acceleration time scale ($t_{\text{acc}} = 6E_{\text{p}}c/eBv_{\text{sh}}^2$) [83, 104], B being the magnetic field strength. The magnetic field is inversely proportional to the shock radius r and it is $B = 3/2(4\pi\epsilon_{\text{B}}m_{\text{p}}n_{\text{in,CSM}}v_{\text{sh}}^2)^{1/2}(r_{\text{in}}/r)$, where ϵ_{B} is the fraction of the post shock thermal energy that goes into the magnetic field [83, 105, 106]. A detailed analysis on the effects of magnetic field on $E_{\text{p,max}}$ can be found in Ref. [107].

The energy losses suffered by relativistic protons mainly come from two competing processes, due to the adiabatic expansion of the shock shell and the pp interactions with the CSM protons. The adiabatic loss time scale or the dynamical time scale is $t_{\text{ad}} \sim t_{\text{dyn}} = r/v_{\text{sh}}$ and the pp collision time scale is $t_{\text{pp}} = [4\kappa_{\text{pp}}\sigma_{\text{pp}}n_{\text{CSM}}(r)c]^{-1}$, where $\kappa_{\text{pp}} = 0.5$ is the proton inelasticity and σ_{pp} is the pp interaction cross-section. We assume $\sigma_{\text{pp}} \approx 3 \times 10^{-26} \text{ cm}^2$, neglecting the energy dependence of σ_{pp} since it hardly affects t_{pp} [19, 83] (however, as specified later, we include the energy dependence in σ_{pp} for the calculation of the secondaries). In addition, protons undergo other energy loss processes, as detailed in Appendix A. Thus, $E_{\text{p,max}}$ can be estimated from $t_{\text{acc}} = 6E_{\text{p,max}}c/eBv_{\text{sh}}^2 = \min[t_{\text{pp}}, t_{\text{ad}}]$ and changes according to the radial evolution of the background environment.

The radial evolution of the steady state proton number, $N_{\text{p}}(E_{\text{p}}, r)$ is described by the following equation [19, 83, 96, 108, 109]:

$$\frac{\partial N_{\text{p}}(E_{\text{p}}, r)}{\partial r} + \frac{N_{\text{p}}(E_{\text{p}}, r)}{v_{\text{sh}}t_{\text{pp}}(r)} - \frac{\partial}{\partial E_{\text{p}}} \left[\frac{E_{\text{p}}N_{\text{p}}(E_{\text{p}}, r)}{r} \right] = N_{\text{p}}^{\text{inj}}(E_{\text{p}}, r), \quad (2.4)$$

where the second term on the left hand side corresponds to energy losses via pp collisions and the third term stands for adiabatic losses. This primary steady state proton number drives the production of the secondary neutrinos and gamma-rays. The time evolution of the fluxes can be probed from the relation between the shock radius and the shock velocity: $r = v_{\text{sh}}t$.

2.2 Gamma-ray production

Gamma-rays can be produced through pp interactions via decay of neutral π and η mesons, with the following decay channels: $\pi^0 \rightarrow 2\gamma$, $\eta \rightarrow 2\gamma$, $\eta \rightarrow 3\pi^0$, $\eta \rightarrow \pi^+\pi^-\pi^0$, and $\eta \rightarrow \pi^+\pi^-\gamma$ [44]. The radial evolution of gamma-rays with energy E_{γ} produced in pp collisions can be computed as follows [93, 110]:

$$\frac{dN_{\gamma}(E_{\gamma}, r)}{dr} + \frac{N_{\gamma}(E_{\gamma}, r)}{v_{\text{sh}}t_{\text{esc}}} = N_{\gamma}^{\text{inj}}(E_{\gamma}, r), \quad (2.5)$$

where $t_{\text{esc}} = r/4c$ is the escape time of secondary particles. The factor 4 corresponds to the compression of the CSM due to shock pressure [96]. The source term, $N_{\gamma}^{\text{inj}}(E_{\gamma}, r)$, below $E_{\text{p}} = 0.1 \text{ TeV}$ is given by [44]

$$N_{\gamma}^{\text{inj}}(E_{\gamma}, r) = 2 \frac{\tilde{\eta}}{K_{\pi}} \frac{4cn_{\text{CSM}}(r)m_{\text{e}}}{v_{\text{sh}}m_{\text{p}}} \int_{E_{\text{min}}}^{\infty} \frac{dE_{\pi}}{\sqrt{E_{\pi}^2 - m_{\pi}^2}} \sigma_{\text{pp}}(E_{\text{p}}) N_{\text{p}}(E_{\text{p}}), \quad (2.6)$$

where $E_{\text{p}} = m_{\text{p}} + E_{\pi}/K_{\pi}$ and $E_{\text{min}} = E_{\gamma} + m_{\pi}^2/E_{\gamma}$. Above $E_{\text{p}} = 0.1 \text{ TeV}$,

$$N_{\gamma}^{\text{inj}}(E_{\gamma}, r) = \frac{4cn_{\text{CSM}}(r)m_{\text{e}}}{v_{\text{sh}}m_{\text{p}}} \int_{m_{\text{p}}}^{\infty} dE_{\text{p}} \frac{\sigma_{\text{pp}}(E_{\text{p}})}{E_{\text{p}}} N_{\text{p}}(E_{\text{p}}, r) F_{\gamma} \left(\frac{E_{\gamma}}{E_{\text{p}}} \right), \quad (2.7)$$

with $F_{\gamma}(E_{\gamma}/E_{\text{p}})$ being the gamma-ray production rate, and E_{γ} the gamma-ray energy. The parameters K_{π} and $\tilde{\eta}$ are free parameters, used for connecting the injection rates above energy $E_{\text{p}} = 1 \text{ TeV}$.

The total gamma-ray flux observed at Earth from a source at luminosity distance d_{L} is given by:

$$\begin{aligned} E_{\gamma}^2 \Phi_{\gamma}(E_{\gamma, \text{obs}}) &= \frac{e^{-\tau_{\gamma, \text{EBL}}(E_{\gamma}, z)}}{4\pi d_{\text{L}}^2} E_{\gamma}^2 \phi_{\gamma}^{\text{s}}(E_{\gamma}) \\ &= \frac{e^{-\tau_{\gamma, \text{EBL}}(E_{\gamma}, z)}}{4\pi d_{\text{L}}^2} \int_{r_{\text{in}}}^{r_{\text{max}}} dr \frac{E_{\gamma}^2 N_{\gamma}(E_{\gamma}, r) e^{-(\tau_{\gamma\gamma} + \tau_{\text{BH}})}}{m_{\text{e}} c^2 t_{\text{esc}} v_{\text{sh}}}, \end{aligned} \quad (2.8)$$

where $E_\gamma = (1+z)E_{\gamma,\text{obs}}$, z is the cosmological redshift and ϕ_γ^s is the gamma-ray flux at source. The maximum shock radius, r_{max} corresponds to the end of particle production (see Sec. 2.3 for details). Here, $\tau_{\gamma\gamma}$ and τ_{BH} are the optical depths for gamma-gamma and Bethe-Heitler interactions, respectively; their modeling is introduced in the following. $\tau_{\gamma,\text{EBL}}(E_\gamma, z)$ is the optical depth for the interaction of gamma-rays with the EBL [94, 111].

The gamma-rays produced in the hadronic processes can interact with the low energy thermal photons present in the CSM [83, 93, 110]. In these interactions, electron-positron pairs can be produced. Electron-positron pairs can also be produced in Bethe-Heitler processes, where high-energy photons interact with nuclei (mostly protons) in the ejecta [110].

The attenuation of the gamma-ray spectra due to photon-photon pair production is taken into account through the factor $e^{-\tau_{\gamma\gamma}}$ in Eq. 2.8; the optical depth $\tau_{\gamma\gamma}$ of the CSM thermal photons is computed as follows

$$\tau_{\gamma\gamma} = r_{\text{max}} \int_0^\infty n_{\text{ph}}(\epsilon) \sigma_{\gamma\gamma}(E_\gamma, \epsilon) d\epsilon, \quad (2.9)$$

where ϵ is the energy of thermal photons and $\sigma_{\gamma\gamma}(E_\gamma, \epsilon)$ is the photon-photon annihilation cross section [110, 112]. The number density of thermal photons follows a black-body spectrum,

$$n_{\text{ph}}(\epsilon) \propto \frac{\epsilon^2}{\exp(\epsilon/T) + 1}, \quad (2.10)$$

where T is the temperature of the thermal photons and can be defined in terms of average energy, ϵ_{av} of photons as $T = \epsilon_{\text{av}}/3.15$. The constant of proportionality is such that

$$\int_0^\infty d\epsilon n_{\text{ph}}(\epsilon) = U_{\text{ph,av}}. \quad (2.11)$$

The average energy density of thermal photons in the CSM is:

$$U_{\text{ph,av}} = \frac{1}{r_{\text{max}}} \int_{r_{\text{in}}}^{r_{\text{max}}} dr \frac{L_{\text{SN,pk}}}{4\pi cr^2}, \quad (2.12)$$

where $L_{\text{SN,pk}}$ is the SN peak luminosity. In general, the energy density of thermal photons scales as $1/r^2$ with the shock radius, r . We take the average energy density of the thermal photons in the interaction zone, i.e. between $r_{\text{in}} \leq r < r_{\text{max}}$, to make a reasonable estimate of the absorption of gamma-rays caused by the thermal photons.

In addition to $\gamma\gamma$ pair production losses, Bethe-Heitler pair production losses can also affect the gamma-ray spectra. The loss due to this process can be estimated by the factor $e^{-\tau_{\text{BH}}}$ in Eq. 2.8, where τ_{BH} is the optical depth. The latter depends on the mass and composition of the ejecta and we model it as in Ref. [110].

The electrons (positrons) produced in these processes may lose energy via synchrotron radiation due to the presence of magnetic fields in the shocked CSM. They also lose energy due to inverse Compton scattering with low-energy photons in the CSM. Electrons and positrons can then annihilate and produce low-energy gamma-rays, which in turn modify the observed gamma-ray spectra. This cascading of electromagnetic (EM) interactions modifying the gamma-ray spectrum can be estimated with a broken power law and is given by [113],

$$\phi_{\gamma,\text{cascade}}(E_\gamma) \propto \begin{cases} E_\gamma^{-1.5} & (E_\gamma < E_{\gamma,\text{b}}) \\ E_\gamma^{-\alpha_\gamma} & (E_{\gamma,\text{b}} < E_\gamma < E_{\text{cut}}) \end{cases} \quad (2.13)$$

where E_{cut} is the cut-off energy defined as $\tau_{\gamma\gamma}(E_\gamma = E_{\text{cut}} = E_{\text{max}}) = 1$, $E_{\gamma,b}$ is the break energy given by $E_{\gamma,b} = 4E_{\text{cut}}^2/3(2m_e c^2)^2 \epsilon_{\text{av}}$ and the power law index $\alpha_\gamma = 2$. This cascaded flux is normalized to the total energy lost above E_{cut} due to pair production. This suggests that the larger the absorption, the larger the cascaded flux. Therefore, harder spectra would produce large cascaded gamma-ray flux.

The primary electrons accelerated in the shock could also produce gamma-rays via inverse Compton. The gamma-ray contribution of pp collisions (i.e., $\pi^0 \rightarrow 2\gamma$) generally dominates in the high-energy range (GeV), hence the gamma ray contribution from the primary electrons can be ignored, see e.g. [93].

2.3 Neutrino production

Neutrinos are produced through the decay of charged pions created in pp interactions, $\pi \rightarrow \mu\nu_\mu$ and $\mu \rightarrow e\nu_e\nu_\mu$. The decay of η mesons also produces neutrinos, but their contribution is smaller than the one of pions [44]. The evolution of neutrinos at different radii is governed by the following equation [19]:

$$\frac{dN_{\nu_f}(E_\nu, r)}{dr} + \frac{N_{\nu_f}(E_\nu, r)}{v_{\text{sh}} t_{\text{esc}}(r)} = N_{\nu_f}^{\text{inj}}(E_\nu, r), \quad (2.14)$$

where $t_{\text{esc}}(r) = r/4c$ is the time required for neutrinos to escape the CSM (see comments below Eq. 2.5). of flavour f ($f = e, \mu$ at the source) with neutrino energy E_ν . The neutrino injection term $N_{\nu_f}^{\text{inj}}(E_\nu, r)$ is obtained by following Ref. [44].

For $E_p < 0.1$ TeV:

$$\begin{aligned} N_{\nu_e}^{\text{inj}}(E_\nu, r) &= 2 \frac{\tilde{\eta}}{K_\pi} \frac{4cn_{\text{CSM}}(r)m_e}{v_{\text{sh}}m_p} \int_{E_{\text{min}}}^{\infty} \frac{dE_\pi}{\sqrt{E_\pi^2 - m_\pi^2}} \sigma_{\text{pp}}(E_p) N_p(E_p, r) f_{\nu_e}\left(\frac{E_\nu}{E_\pi}\right) \\ N_{\nu_\mu}^{\text{inj}}(E_\nu, r) &= 2 \frac{\tilde{\eta}}{K_\pi} \frac{4cn_{\text{CSM}}(r)m_e}{v_{\text{sh}}m_p} \int_{E_{\text{min}}}^{\infty} \frac{dE_\pi}{\sqrt{E_\pi^2 - m_\pi^2}} \sigma_{\text{pp}}(E_p) N_p(E_p, r) \\ &\quad \times \left[f_{\nu_\mu}^{(1)}\left(\frac{E_\nu}{E_\pi}\right) + f_{\nu_\mu}^{(2)}\left(\frac{E_\nu}{E_\pi}\right) \right] \end{aligned} \quad (2.15)$$

where $E_p = m_p + E_\pi/K_\pi$, and E_π is the energy of pion and m_e is mass of electron. The minimum energy of pion is given by $E_{\text{min}} \simeq E_\nu + m_\pi^2/4E_\nu$. The parameters K_π and $\tilde{\eta}$ are free parameters and used for connecting the injection rates above energy $E_p = 1$ TeV.

For $E_p \geq 0.1$ TeV:

$$\begin{aligned} N_{\nu_e}^{\text{inj}}(E_\nu, r) &= \frac{4cn_{\text{CSM}}(r)m_e}{v_{\text{sh}}m_p} \int_{m_p}^{\infty} dE_p \frac{\sigma_{\text{pp}}(E_p)}{E_p} N_p(E_p, r) F_{\nu_e}\left(\frac{E_\nu}{E_p}\right) \\ N_{\nu_\mu}^{\text{inj}}(E_\nu, r) &= \frac{4cn_{\text{CSM}}(r)m_e}{v_{\text{sh}}m_p} \int_{m_p}^{\infty} dE_p \frac{\sigma_{\text{pp}}(E_p)}{E_p} N_p(E_p, r) \\ &\quad \times \left[F_{\nu_\mu}^{(1)}\left(\frac{E_\nu}{E_p}\right) + F_{\nu_\mu}^{(2)}\left(\frac{E_\nu}{E_p}\right) \right]. \end{aligned} \quad (2.16)$$

Here, F_{ν_e} , $F_{\nu_\mu}^{(1)}$, $F_{\nu_\mu}^{(2)}$ and f_{ν_e} , $f_{\nu_\mu}^{(1)}$, $f_{\nu_\mu}^{(2)}$ are the neutrino distributions from pion decay valid for $E_p \geq 0.1$ TeV and $E_p < 0.1$ TeV, respectively [44]. The energy dependent cross-section $\sigma_{\text{pp}}(E_p)$ is taken from Ref. [44]. The neutrino flux of flavour f at source is given by,

$$E_\nu^2 \phi_{\nu_f}^s(E_\nu) = \int_{r_{\text{in}}}^{r_{\text{max}}} \frac{dr}{v_{\text{sh}}} \frac{E_\nu^2 N_{\nu_f}(E_\nu, r)}{m_e c^2 t_{\text{esc}}}. \quad (2.17)$$

The all flavour flux at source is $E_\nu^2 \phi_\nu^s = \sum_f E_\nu^2 \phi_{\nu_f}^s(E_\nu)$. During propagation to Earth, the flavour combination may change due to flavour mixing [114], leading to the following flavour composition at Earth: $\nu_e : \nu_\mu : \nu_\tau = 1 : 1 : 1$.

$$E_{\nu,\text{obs}}^2 \Phi_\nu(E_{\nu,\text{obs}}) = \frac{\sum_f E_\nu^2 \phi_{\nu_f}^s(E_\nu)}{4\pi d_L^2}, \quad (2.18)$$

where $E_\nu = (1+z)E_{\nu,\text{obs}}$ and z is the cosmological redshift.

Note that the neutrino (gamma-ray) production from pp interactions ceases to be significant as the shock radius reaches the maximum radius, r_{max} . This is determined by $\min[r_{\text{dec}}, r_{\text{out}}]$. The deceleration radius, r_{dec} , of the SN shock corresponds to the radius when the ejecta mass, M_{ej} , sweeps up the same amount of CSM mass and is defined as $r_{\text{dec}} = M_{\text{ej}} v_w / \dot{M}_W = r_{\text{in}} + M_{\text{ej}} / (4\pi m n_{\text{in,CSM}} r_{\text{in}}^2)$. The region $r < r_{\text{dec}}$ is known as the free expansion phase of the CSM. Particle acceleration and production are dominant in this phase. Once the shock reaches the maximum radius i.e., r_{max} , the interaction of the shock with the ISM begins, which is beyond the scope of this work⁴.

Most SNe show signs of interaction within a few years of their evolution with rarer cases showing interaction on timescales of $\mathcal{O}(10)$ years, see e.g. Refs. [115–120]. Since the maximum time, t_{max} (corresponding to r_{max}) depends on the extent of the CSM, YSNe with extended CSM could have $t_{\text{max}} \sim \mathcal{O}(10)$ years. However, this extended CSM is less dense than the CSM of $t_{\text{max}} \simeq 1$ year. Therefore, the neutrino and gamma-ray fluxes for this extended CSM are similar to that of YSNe with CSM of 1 year (results not shown here). Therefore, we take $r_{\text{max}} = r_{\text{out}}$ (corresponds to $t_{\text{max}} = 1$ year) throughout this work.

Different classes of YSNe produce different fluxes of secondaries (gamma-rays and neutrinos) due to wide differences in these input parameters. In the following, we discuss the different Types of YSNe and their impact on the secondary production.

3 Young supernova types

Supernovae are classified as Type-I and Type-II based on the presence of H lines in the observed spectra. Type-I SNe do not show H lines, whereas Type-II do. Supernovae are further classified into different sub-Types of Type-I (Ia, Ib and Ic) and Type-II (IIn, II-P, I Ib, II-L) SNe depending on different observed characteristics. Type Ia SNe show Silicon II (Si II) absorption lines in their spectra. Presence of He lines in Type Ib SNe differentiates them from Type Ic. Type IIn and IIb exhibit narrow and broad H lines respectively. The spectra of Type II-P SNe show a plateau whereas Type II-L SNe show linearly declining spectra (for details on SN classification, see e.g. Refs. [88, 89]). Except for SNe Ia, all other SN classes are powered by the collapse of the stellar core.

The diverse classes of YSNe differ in parameters like mass loss rate, wind velocity, size of the CSM, and efficiency of shock energy transfer to protons. Below we report about these characteristic parameters as from electromagnetic observations for different Types of YSNe.

- Type IIn SNe are found to have very dense CSM as a result of heavy mass loss (10^{-4} – $10^1 M_\odot \text{yr}^{-1}$) before explosion [67, 121]. The wind velocity, v_w , for such SNe can typically vary between 30–600 kms^{-1} [67]. Their progenitors are not well known and have been

⁴In the case of old SNR (> 1 kyr), the flux due to the Sedov-Taylor phase ($r > r_{\text{dec}}$) decreases by several (more than 3–4) orders of magnitude due to the very low target (CSM or ISM) density. Thus, the total flux from the Sedov-Taylor phase will be negligible compared to the early YSN phase.

found to be connected to LBV, Red Supergiant (RSG) and Yellow Hypergiant (YHG) stars (see e.g., [122–125] and references therein). These stars have large mass loss rates ($\dot{M}_W \sim 10^{-3}$ – $10^1 \text{ M}_\odot \text{ yr}^{-1}$) and moderate wind velocity ($v_w \sim 100 \text{ km s}^{-1}$) [67, 121]. Therefore, Type IIn SNe show a dense CSM ($n_{\text{in,CSM}} \sim 10^{11} \text{ cm}^{-3}$ [67]). Their shock velocity, v_{sh} , ranges between 10^3 and 10^4 km s^{-1} [19, 78, 101] (see Eq. 2.1). The fraction of kinetic energy, ϵ_p , that goes into high energy protons is estimated to be 10^{-2} – 1.5×10^{-1} [103]. Therefore, we choose the range of ϵ_p as 10^{-2} – 10^{-1} . The fraction of post-shock magnetic energy, ϵ_B , can be constrained from radio observations of SNe and is in the range $\epsilon_B \sim 10^{-4}$ – 10^{-2} [78, 81, 126, 127].

- Type II-P SNe show a plateau in their light curves up to a few months (~ 20 – 100 days) after the explosion [128, 129]. This is due to the abundance of hydrogen in the SN ejecta. This SN class usually arises from red supergiant (RSG) stars [67, 130–133] and they are found to have large CSM density. Eruptive mass losses of such stars just before $\mathcal{O}(1)$ year the SN explosion are believed to be the reason of their large CSM densities [128, 134]. The typical mass loss rate during this phase has been reported to be $\mathcal{O}(10^{-3}) \text{ M}_\odot \text{ yr}^{-1}$ [134–136] with wind velocity of $\mathcal{O}(10) \text{ km s}^{-1}$ [137]. Larger mass loss rates [$\mathcal{O}(1) \text{ M}_\odot \text{ yr}^{-1}$] with wind velocity 100 km s^{-1} have also been predicted, see [128, 129]; however, this might be an exception (see e.g., [75, 138, 139])⁵. Interestingly, our calculation only depends on the ratio \dot{M}_W/v_w (see Eq. 2.1); hence, given the evidence of large mass loss rates, we adopt $10^{-2} \text{ M}_\odot \text{ yr}^{-1}$ as our typical mass loss rate with wind velocity $\mathcal{O}(100) \text{ km s}^{-1}$ [129, 134]. This choice is equivalent to assume a mass loss rate $10^{-3} \text{ M}_\odot \text{ yr}^{-1}$ with wind velocity 10 km s^{-1} .

The eruptive mass loss is responsible for a dense CSM which is found to exist up to $\sim 10^{15} \text{ cm}$ [135]. The CSM density beyond this radius is smaller and is due to the stellar wind of RSG stars [67]. A typical RSG wind has a mass loss rate in the range 10^{-6} – $10^{-5} \text{ M}_\odot \text{ yr}^{-1}$ with wind velocities of about 10 – 20 km/s [67]. We distinguish these two different phases of the CSM by naming them “eruptive” (for the large mass loss rates) and “normal” (the smaller RSG winds). The shock velocity for this YSN class is $\mathcal{O}(10^4) \text{ km/s}$ [136].

- Type II-L SNe have linear light curves, while Type II-b show broad He lines in their spectra. Their progenitors have similar mass loss rates, which lie in the range 10^{-5} – $10^{-4} \text{ M}_\odot \text{ yr}^{-1}$ and have wind velocity between 2×10^1 – 10^2 km s^{-1} [67, 75, 140–144]. The shock velocity for these Types of SNe is found to be of the order of 10^4 km/s [145].
- Type Ib/c SNe are rich in helium (He) and usually have lower mass loss rates (10^{-7} – $10^{-4} \text{ M}_\odot \text{ yr}^{-1}$) than IIn and II-P SNe [67, 77, 146, 147]. The wind velocity for Ib/c SNe is very large ($v_w \sim 10^3 \text{ km s}^{-1}$). Moreover, the inner radius of the CSM is small ($r_{\text{in}} \simeq 10^{12} \text{ cm}$, corresponds to the size of the progenitor). This implies that the volume of the CSM shell in the vicinity of r_{in} is also small and therefore the total number of proton targets is quite low. Thus, the neutrino and gamma-ray emission from such YSNs is negligible (as most of the secondaries are produced near r_{in}). However, late time observations of SN 2014C (which was initially classified as Ib/c SN) highlight the presence of interaction of the SN ejecta with the hydrogen rich CSM at $6 \times 10^{16} \text{ cm}$ [137].

⁵Ref. [129] investigated early light curves of some Type II SNe. Their results suggest the need for local CSM ($r < 2 \times 10^{14} \text{ cm}$) in order to reproduce the rapid rise time and brighter emission at peak observed in some SNe. This is an exception and we therefore focus on the average mass loss over a longer period of time.

Table 1. Characteristic parameters for different YSN Types. We consider two different phases of the CSM of II-P SNe namely, eruptive (created by the large mass loss occurring a few years prior to explosion) and normal (due to the usual RSG wind during stellar evolution).

Parameters	IIIn (1 yr)	II-P		IIb/II-L (1 yr)	Ib/c (1 yr)	Ib/c (LT) (1.5 yrs)
		Eruptive (≤ 12)	Normal (> 12 days)			
$n_{\text{in,CSM}}$ (cm^{-3})	10^{11}	10^{12}	10^9	6×10^{11}	2.4×10^{12}	2×10^6
\dot{M}_W ($M_\odot \text{ yr}^{-1}$)	10^{-1}	10^{-2}	2×10^{-6}	3×10^{-5}	10^{-5}	2×10^{-2}
v_w (kms^{-1})	10^2	10^2	1.5×10^1	3×10^1	10^3	10^2
r_{out} (cm)	2×10^{16}	10^{15}	3×10^{16}	3×10^{16}	6×10^{16}	10^{17}
v_{sh} (kms^{-1})	7×10^3	10^4	10^4	10^4	2×10^4	10^4
r_{in} (cm)	4×10^{14}	6×10^{13}	6×10^{13}	6×10^{12}	3×10^{11}	5×10^{16}
ϵ_p	10^{-2}	10^{-1}	10^{-1}	10^{-1}	10^{-1}	5×10^{-2}
ϵ_B	10^{-2}	10^{-2}	10^{-2}	10^{-2}	10^{-2}	10^{-2}

The CSM is found to extend up to 2.5×10^{17} cm [148]; hence, we assume $r_{\text{out}} = 10^{17}$ cm. This corresponds to the beginning of shock interaction at about 1.5 years after the explosion and substantial reduction of the dense CSM interaction at about 3 years. Thus the duration of emission is considered to be about 1.5 years. This dense CSM is possibly created by large mass loss rate of $\mathcal{O}(1) M_\odot \text{ yr}^{-1}$ with wind velocity in the range ($10^1 - 10^3 \text{ km s}^{-1}$) [137]. However, smaller mass loss rate of $\mathcal{O}(10^{-3}) M_\odot \text{ yr}^{-1}$ with velocity 100 km s^{-1} has also been proposed [149]. Hence, we assume a mass loss rate of $\mathcal{O}(10^{-2}) M_\odot \text{ yr}^{-1}$ and wind velocity 100 km s^{-1} to be conservative. The exact mechanism of this large mass loss is not well understood. Therefore, we assume a wind profile in order to obtain a conservative estimate of the CSM density. The deceleration radius, r_{dec} (9×10^{16} cm) of the shock moving forward in the CSM is comparable to r_{out} . SN 2004dk and SN2019yvr are similar examples of Ib/c SN with late time interaction after explosion [150, 151]. Reference [137] investigated a sample of 183 Ib/c SNe and found that 10% of the sample has late time interaction like SN2014C, which is about 2.6% of the total core-collapse SNe. Hence, we include late time interaction of Ib/c SNe in our analysis. We choose the SN 2014C as a representative of the class Type Ib/c late time (LT) SN [93, 137, 149, 152].

In Table 1, we list the typical values adopted for each of our modelling parameters for all SN Types introduced above. While we chose to be conservative in our choice of the characteristic parameters, we also consider a range of variability for the most uncertain model parameters and the latter defines a band in the final results (see Sec. 5 and 2).

4 Dependence of the gamma-ray and neutrino emission on the young supernova type

The YSN emission properties largely vary across different SN Types. In this Section, we first characterize the gamma-ray and neutrino emission for our benchmark YSN IIIn and then compare the particle production across different YSN classes. Throughout this Section, the emission of secondaries is computed for 1 year for all YSN Types, except for Ib/c (LT) YSNe for which we consider an emission period of 1.5 years.

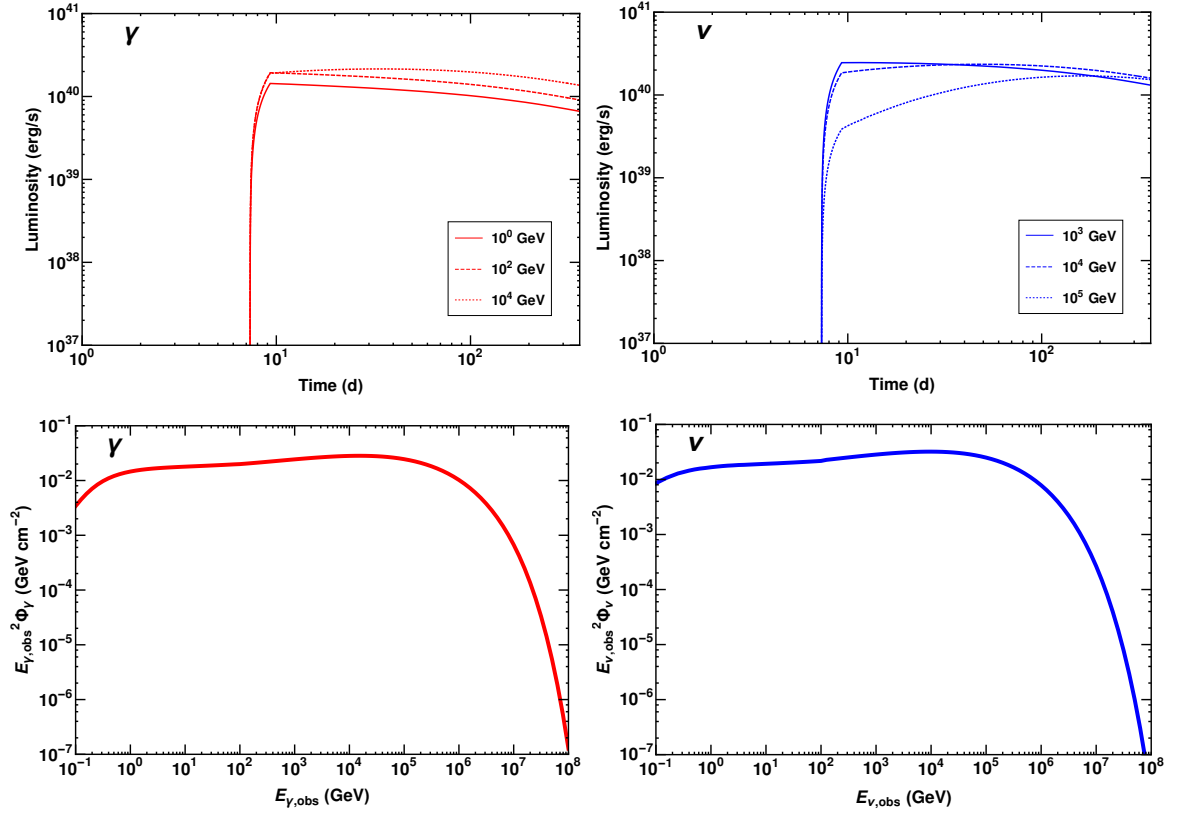


Figure 1. *Top panels:* Luminosity of gamma-rays (left) and all-flavour neutrinos (right) of our benchmark YSN IIn (see Table 1) as a function of time. The temporal evolution at the source are shown for three representative energies ($E_{\gamma} = 10^0, 10^2$, and 10^4 GeV for gamma-rays and $E_{\nu} = 10^3, 10^4$, and 10^5 GeV for neutrinos). *Bottom panels:* Corresponding gamma-ray (left) and all-flavour neutrino (right) fluences at Earth as functions of the observed particle energy. The distance of our YSN IIn from Earth is chosen to be 10 Mpc. Both fluences for neutrinos and gamma-rays are time integrated over the first year of the SN evolution. Gamma-rays are shown without any attenuation due to energy losses (see discussion of Fig. 2 for details). Therefore, the spectra of both species from pp collision follow a similar behaviour of growing with particle’s energy and falling rapidly above 10^5 GeV.

4.1 Characteristic gamma-ray and neutrino emission

As a primary example to illustrate the YSN neutrino and gamma-ray emission we consider Type IIn SNe (see Sec. 2 and Table 1) as they have the highest mass loss rate in the SN sample presented in Table 1. Unless otherwise specified, we assume that our benchmark YSN is located at 10 Mpc from Earth. Most SNe are detected between 1 and 100 Mpc, with the majority being discovered at $\mathcal{O}(90)$ Mpc, see e.g. Fig. 2 of Ref. [153]. Hence, our choice of the typical SN distance is somewhat optimistic, yet compatible with observations.

The top and bottom left (right) panels of Fig. 1 show the gamma-ray (neutrino) luminosity and fluence. The top left panel shows the gamma-ray light curve at $E_{\gamma} = 1, 10^2, 10^4$ GeV, while the gamma-ray fluence produced by pp collisions in IIn YSNe during its first year is displayed in the bottom left panel. The fluence in the bottom left panel of Fig. 1 does not include any attenuation at the source. Gamma-rays above 100 GeV can interact with low energy photons and ambient matter in the source and may get lost. This corresponds to

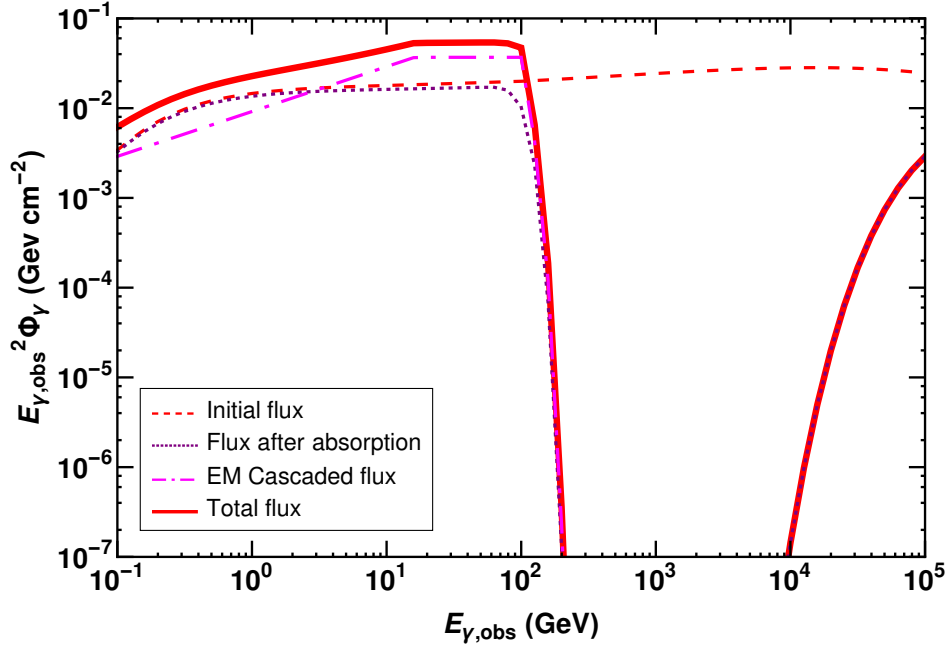


Figure 2. Gamma-ray fluence at Earth after including the relevant absorption processes and EM cascades at the source as a function of the gamma-ray energy for our benchmark YSN IIn (see Table 1) at a distance of 10 Mpc. The red-dashed curve represents the fluence obtained via pp collisions. The purple-dotted curve is the fluence after absorption due to $\gamma\gamma$ pair production loss and Bethe-Heitler loss in the CSM. The gamma-ray fluence due to EM cascades is shown by the dot-dashed magenta curve. The thick red solid curve represents total flux at the source after absorption and EM cascades. The gamma-ray fluence between 10^2 to 10^4 GeV is heavily attenuated due to the absorption processes occurring in the source. The final gamma-ray flux (thick red curve) is a combination of the flux surviving to absorption and the EM cascaded flux.

$\tau_{\gamma\gamma}$ and τ_{BH} , respectively, in Eq. 2.8 and are discussed below (see discussion of Fig. 2).

The top panel on the right shows the neutrino light curve (blue) for three different energies ($E_\nu = 10^3, 10^4, 10^5$ GeV) for the first year of the YSN. The light curves start around 7 days after the explosion. This delay corresponds to the inner radius, r_{in} (i.e., when the interaction between the shock wave accelerated protons and the CSM protons has begun). The inner radius, r_{in} , also depends on the class properties of each SN Type. The plot in the bottom right panel shows the energy spectra of the YSN emitted neutrinos for the first year. The neutrino flux (top right plot) falls rapidly above energy $E_\nu \sim 10^5$ GeV. This is due to the maximum energy of protons $E_{\text{p,max}}$, which determines the exponential cut-off of the proton spectra. This clearly suggests that the SN properties driving $E_{\text{p,max}}$ will influence the cut-off, and the latter would be different for different YSN Types. Note that these interpretations also hold for the gamma-rays in the left panel.

The fluence in the bottom left panel of Fig. 1 will be affected by absorption processes. Fig. 2 shows the effect of absorption and EM cascades on the gamma-rays produced via pp interactions for Type IIn YSNs for a thermal energy distribution of photons with average energy $\epsilon_{\text{av}} = 1$ eV and SN peak luminosity $L_{\text{SN,pk}} = 10^{41}$ erg/s respectively [83, 154]. We show gamma-rays without any absorption (red-dashed curve), gamma-rays with absorption due to photon-photon pair production and BH pair production (purple-dotted curve), and

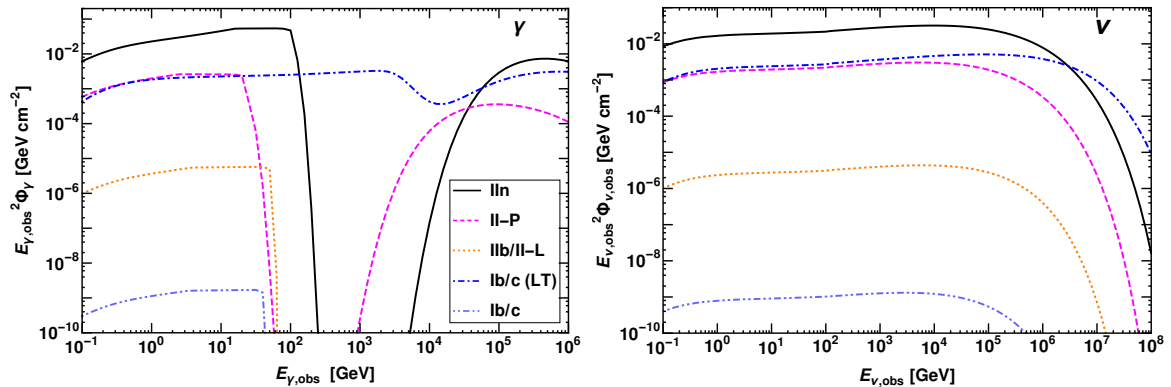


Figure 3. Gamma-ray (left) and all-flavour neutrino (right) fluences integrated for a year at Earth from different classes of YSN, as listed in Table 1, for a source located at 10 Mpc. For both gamma-rays and neutrinos, Type IIn YSNe have the largest fluence, followed by II-P and Ib/c (LT) YSNe.

the EM cascade (magenta dot-dashed curve). It is interesting to note that the initial flux above 200 GeV mostly disappears except a little tail at higher energies due to photon-photon pair production losses. This is due to the fact that the photon-photon cross section $\sigma_{\gamma\gamma}$ falls rapidly at higher energies and the thermal photons, $n_{\text{ph}}(\epsilon)$, have a black-body spectrum; the product of both gives rise to an optical depth, $\tau_{\gamma\gamma}$ creating a well-shaped attenuation factor $e^{-\tau_{\gamma\gamma}}$. The cascaded gamma-ray flux also falls sharply at 200 GeV because the photon-photon pair loss factor $e^{-\tau_{\gamma\gamma}}$ hardly allows for anything to survive above 200 GeV.

Bethe-Heitler losses generally have a tiny effect on the gamma-ray energy distribution. For Type IIn SNe, the amount of attenuation is the small gap between the red-dashed and the purple dotted curve below 200 GeV. Thus the final gamma-ray flux (thick red curve) is a combination of the flux surviving to absorption (purple dotted) and EM cascaded flux (magenta dot-dashed). The EM cascades are responsible for a boost in the gamma-ray spectra below 200 GeV. Propagation to Earth is not important at 10 Mpc but important for large distances (~ 1 Gpc) as losses due to EBL will take place, for example for the diffuse flux (see Sec. 5).

4.2 Dependence on the young supernova type

Because of the intrinsic differences among the properties of the YSN Types introduced in Sec. 3, we should expect a wide variation in the emission of secondary particles. Below we discuss a few examples of these variations for the secondary gamma-rays and neutrinos for a source at 10 Mpc and $\alpha_p = 2.0$.

We show the gamma-ray fluences produced by YSNe in the top left panel of Fig. 3 for the benchmark parameters shown in Table 1. The fluxes are integrated over a year. Type IIn YSNe produce the largest gamma-ray fluence. The other Types of YSNe create smaller fluences and the fluence of Type Ib/c YSNe is extremely small relative to the one seen from the Type IIn YSNe. The sharp fall and rise of these fluences at higher energies (above 10 GeV) is due to the fact that gamma-rays suffer losses due to $\gamma\gamma$ pair production, as discussed in Sec. 2.2. The fall and rise of the fluences occur at different energies according to the YSN class. The amount of losses are also different for different YSNe. This is due to the variation of the parameters, i.e. average energy (ϵ_{av}) and peak luminosity ($L_{\text{SN,pk}}$) of thermal photons expected from different Types of YSNe. The parameter ϵ_{av} is assumed

to be: 1 eV for IIn YSNe, 4.5 eV for II-P YSNe, 1 eV for IIb/II-L and Ib/c YSNe, and 0.05 eV for Ib/c (LT) YSNe. The peak luminosities are assumed to be 10^{41} erg/s for IIn SNe, $\sim 5 \times 10^{40}$ erg/s for II-P and Ib/c (LT) SNe, and 10^{42} erg/s for IIb/II-L and Ib/c SNe [83, 93, 135, 145, 155–157]. The fluence of Type Ib/c (LT) YSN falls at higher energy than that of other SN Types due to its small average energy of thermal photons. The average energy is small because of the lower temperature of thermal photons as the CSM is located very far away (see Table 1) from the stellar envelope. The large distance to the CSM also affects the density of the thermal photons that results in less absorption of gamma-rays for Type Ib/c (LT) YSNe. Type IIn and II-P YSNe have similar losses as the peak luminosities of thermal photons are quite similar. Heavy losses of gamma-rays are seen for Type IIb/II-L and Ib/c YSNe because their thermal photon luminosity is quite large which implies large thermal photon density.

The right panel of Fig. 3 shows the corresponding neutrino fluence integrated over a year for the different YSN Types. Due to the dense CSM, Type IIn YSNe show the largest fluence falling rapidly around $E_\nu \sim 10^6$ GeV. The fluence of Type Ib/c (LT) YSNe starts to dominate above $E_\nu \sim 3 \times 10^6$ GeV. The reason is that the maximum proton energy ($E_{p,\max}$) strongly depends on the shock velocity and shock radius. The shock velocity and shock radius for Ib/c (LT) YSNe are larger than those of Type IIn YSNe, resulting in greater $E_{p,\max}$. The fluence of Type II-P⁶ and Ib/c (LT) YSNe are comparable at lower energies due to their dense CSM. The fluences of Type IIb/II-L and Type Ib/c YSNe are quite small in spite of the large initial CSM density, $n_{\text{in,CSM}}$. This is due to the small size of their inner radius (r_{in}) of the CSM; moreover, most of the secondaries are only produced in the vicinity of r_{in} .

The estimated neutrino fluences for the various YSNe classes are comparable to the ones reported in Ref. [84] except for the ones of Type II-P YSNe. In this case, our YSNe-IIP fluence is larger⁷ since it relies on model parameters extrapolated from more recent observations of II-P SNe, as discussed in Sec. 3; specifically, the mass loss rate that we adopt is one order of magnitude larger than the one assumed in Ref. [84]. On the other hand, a CSM density smaller than our benchmark case in Table 1 would result in a smaller fluence [84]. In addition, the neutrino emission from Ib/c (LT) SNe is explored for the first time in this paper.

Fig. 4 shows the total energy emitted in gamma-rays (left) and neutrinos (right) for each YSN Type, in order to favour a comparison among their overall energetics. We have integrated the gamma-ray and neutrino fluxes in the energy range 10^{-1} – 10^8 GeV for a year. Both for gamma-rays and neutrinos, the largest energy is emitted by Type IIn YSNe, followed by Type Ib/c (LT) and II-P YSNe. By looking at the fluxes of neutrinos and gamma-rays in Fig. 3, one might have the impression that the total energy emitted in gamma-rays is smaller than that of neutrinos due to the large absorption of gamma-rays (the dips). However this is not the case, most of the attenuated high energy gamma-ray flux has reappeared at lower energies due to the EM cascades (see Fig. 2 and discussion) determining an overall small amount of loss. If there is no absorption of gamma-rays, the total energy of neutrinos is larger by a factor of about 3/2 than that of gamma-rays. This corresponds to the product of charged to neutral pion production ratio (2) and the fraction of energy carried by the

⁶The fluences of Type II-P (gamma-rays and neutrinos) are dominated by the emission from the eruptive phase (see Table 1), the contribution from the normal phase is negligible.

⁷Note that the large mass loss rates of II-P SNe discussed in Ref. [129] may be responsible for a fluence comparable to the one of IIn YSNe [158, 159]. However, such mass loss rates might be an exception, as we discussed in Sec. 3 and therefore we do not consider them.

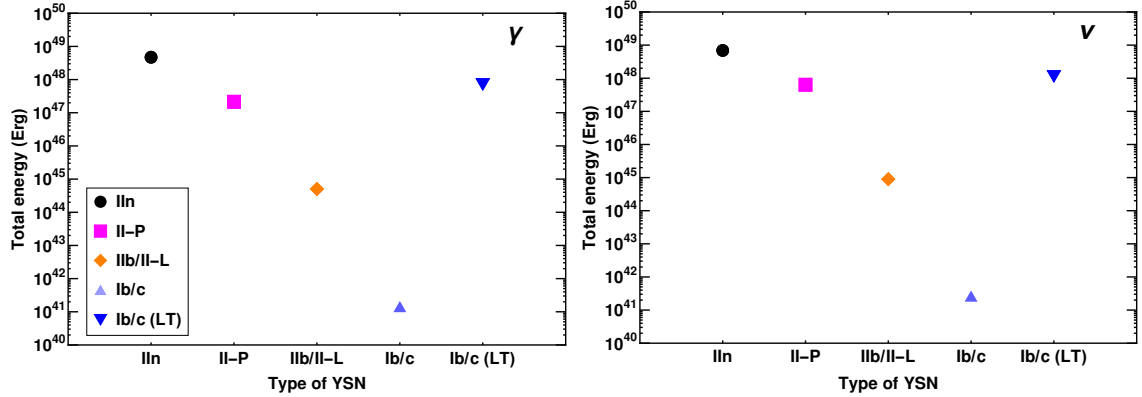


Figure 4. Total energy emitted by each source in gamma-rays (left) and neutrinos (right). The duration of emission of secondary particles is taken to be a year and integrated in the range 10^{-1} – 10^8 GeV. The total energy emitted in gamma-rays is generally smaller than that of neutrinos; this is due to the attenuation of gamma-rays in the source. The largest energy is emitted by Type IIn YSNe, followed by Type Ib/c (LT) and II-P YSNe.

neutrinos in a charged pion decay (3/4).

5 Diffuse gamma-ray and neutrino backgrounds from young supernovae

In this Section, we first introduce the procedure adopted to compute the diffuse backgrounds of high-energy particles. Then, we present our results on the gamma-ray and neutrino diffuse backgrounds from YSNe. A discussion on the model uncertainties and comparison with existing data follows.

5.1 Diffuse flux and its ingredients

The differences among the different YSNe classes for what concerns the emission of secondaries give rise to interesting questions regarding the contribution of each YSN class to the diffuse emission of gamma-rays and neutrinos. In addition to the individual YSN fluxes, the diffuse flux of secondary particles embeds the contribution from the redshift dependence of the various YSNe Types ⁸:

$$E_{j,\text{obs}}^2 \phi_{j,\text{diff}}(E_{j,\text{obs}}) = \zeta \frac{c}{H_0} \int_0^{z_{\text{max}}} dz \frac{R_{\text{CCSN}}(z) E_j^2 \phi_j^s(E_j)}{\sqrt{\Omega_m(1+z)^3 + \Omega_\Lambda}} e^{-\tau_{j,\text{EBL}}(E_j, z)}, \quad (5.1)$$

where, $j = \nu$ or γ , $E_j = (1+z)E_{j,\text{obs}}$ and $\tau_{j,\text{EBL}}(E_j, z)$ is optical depth of EBL. For neutrinos, $\tau_{\nu,\text{EBL}} = 0$. For gamma-rays, the optical depth $\tau_{\gamma,\text{EBL}}$ is taken from Ref. [94]. We adopt the Λ CDM cosmological model, with $\Omega_m = 0.31$, $\Omega_\Lambda = 0.69$, and $H_0 = 68 \text{ km s}^{-1} \text{ Mpc}^{-1}$ [162].

The fraction of different SN Types may vary with redshift due to the change in density of stars and metallicity of the host galaxies seen at higher redshifts. However, unfortunately, the redshift distribution of SNe of different Types is quite uncertain, and limited information is available up to $z = 1$, for some SN Types, which is not sufficient for our purposes [161].

⁸We assume a constant luminosity function based on the benchmark parameters introduced in Table 1, in light of the existing observational uncertainties [160, 161].

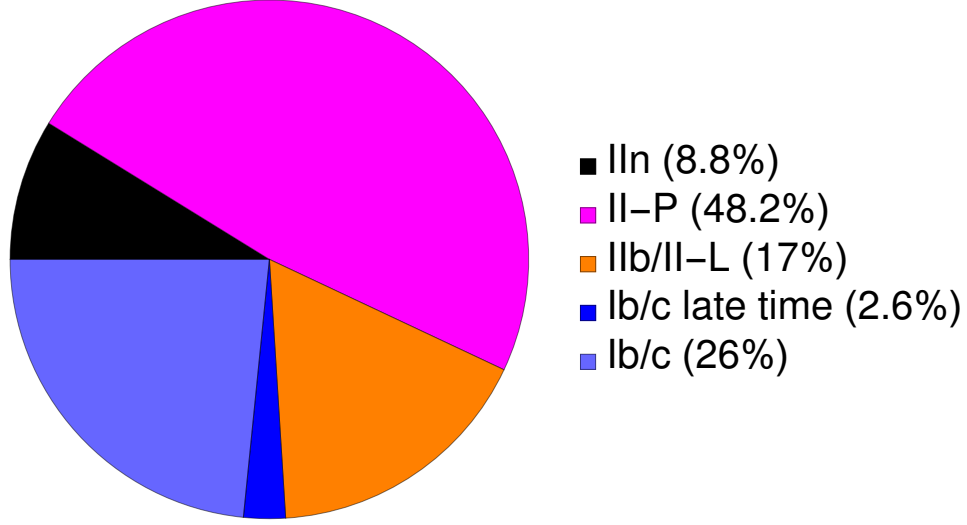


Figure 5. Local rate of core-collapse SNe [160]. Type II-P SNe are the most abundant ones at $z = 0$. Type Ib/c and IIb/II-L SNe are also more frequent than Type IIIn SNe. We assume Type Ib/c (LT) SNe to be 10% of SNe Ib/c [137]; the total rate of SNe Ib/c (i.e., 26%) includes the one of Ib/c (LT) SNe.

Hence, we assume that all SN Types follow the core-collapse SN rate as a function of the redshift. In addition, in order to take into account that some SN Types are more common than others, we follow Ref. [160] and assume that the fraction of different core-collapse SN Types at $z = 0$ (ζ) holds at higher z as well. The fraction of different SN Types at $z = 0$ is shown in Fig. 5.

The rate of core-collapse SNe is given by [163–165]:

$$R_{\text{CCSN}}(z) = \int_{8M_{\odot}}^{125M_{\odot}} dM R_{\text{SN}}(z, M), \quad (5.2)$$

where

$$R_{\text{SN}}(z, M) = \frac{\eta(M)}{\int_{0.5M_{\odot}}^{125M_{\odot}} dM M \eta(M)} R_{\text{SFR}}(z), \quad (5.3)$$

with $\eta(M) \propto M^{-2.35}$ being the initial mass function (following the Salpeter law) [166]. The star formation rate R_{SFR} is [167],

$$R_{\text{SFR}}(z) = C_0 \left[(1+z)^{p_1 k} + \left(\frac{1+z}{5000} \right)^{p_2 k} + \left(\frac{1+z}{9} \right)^{p_3 k} \right]^{1/k}, \quad (5.4)$$

where $k = -10$, $p_1 = 3.4$, $p_2 = -0.3$ and $p_3 = -3.5$. The constant of proportionality C_0 is determined by normalizing the SN rate to the local SN rate as $\int_{8M_{\odot}}^{125M_{\odot}} dM R_{\text{SN}}(0, M) = 1.25 \pm 0.5 \times 10^{-4} \text{ Mpc}^{-3} \text{ yr}^{-1}$ [168].

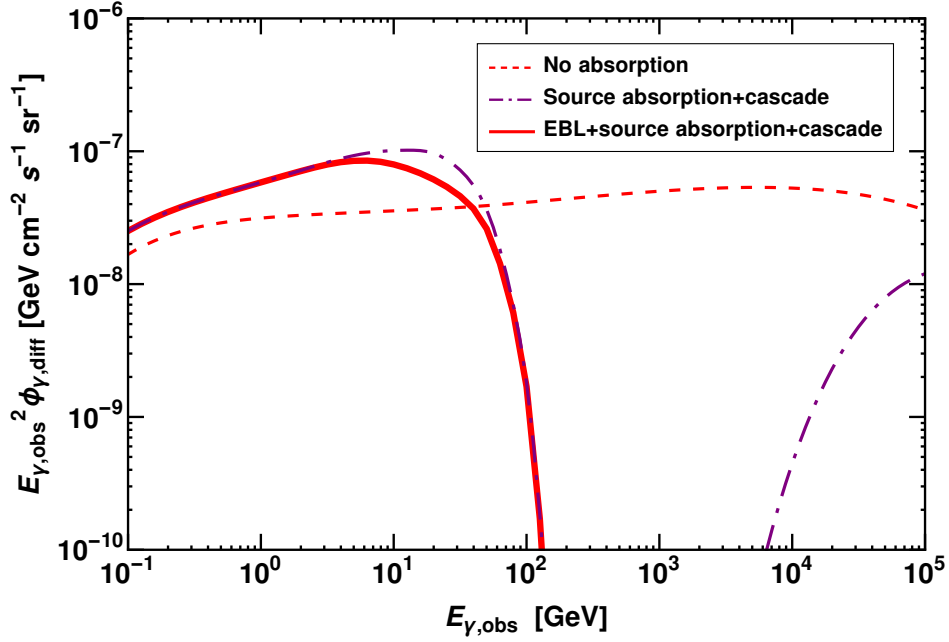


Figure 6. Diffuse gamma-ray flux at Earth for our benchmark Type II_n YSN (see Table 1). The red dashed curve corresponds to the diffuse gamma-ray flux without any absorption. The purple dot-dashed curve shows the diffuse flux after losses ($\gamma\gamma$ and Bethe-Heitler) and EM cascade at source. The final gamma-ray flux at Earth after EBL absorption is represented by the thick red solid curve. EBL absorption is more pronounced above 100 GeV. Moreover, the propagation loss in the diffuse flux has attenuated the higher energy tail above 10^4 GeV. Thus, the final diffuse flux peaks at around 10 GeV and ends abruptly around 100 GeV.

5.2 Diffuse background of gamma-rays

The diffuse background of gamma-rays from YSN can be computed by relying on Eq. 5.1. Because of $\gamma\gamma$ interactions occurring between YSN gamma-rays and the EBL, losses similar to the ones occurring in the source, and discussed in Sec. 2.2, can take place. Substantial EBL losses can affect the high-energy tail of the gamma-ray spectral distribution, while gamma-rays travel over large distances. For example, a 300 GeV gamma-ray photon would need to travel about 1 Gpc to be attenuated by an amount of $1/e$ [94].

In order to compute the amount of EBL absorption, one needs to know the redshift dependence of the EBL for different energies [94, 111, 169, 170]. In this paper, we model $\tau_{\gamma,EBL}(E_\gamma)$ (see Eq. 5.1) following Ref. [94].

Fig. 6 shows the diffuse gamma-ray background for Type II_n YSN ($\zeta \approx 0.9$, see Fig. 5) as a function of the observed photon energy. The red-dashed curve shows the gamma-rays produced through pp interactions (without any energy loss). The purple dot-dashed curve shows the diffuse flux with source absorption and EM cascade, where the small part of the flux at higher energies (above 10^3 GeV) for the purple dot-dashed curve is due to the $\gamma\gamma$ cross-section as discussed in Sec. 2.2. The red solid curve represents the gamma-ray flux after taking into account all the absorption (source+EBL) processes and EM cascades. The purple dot-dashed and red solid curves are larger than the dashed red curve (no absorption) below 100 GeV because of the additional cascaded flux.

The left panel of Fig. 7 displays the diffuse gamma-ray background for the different

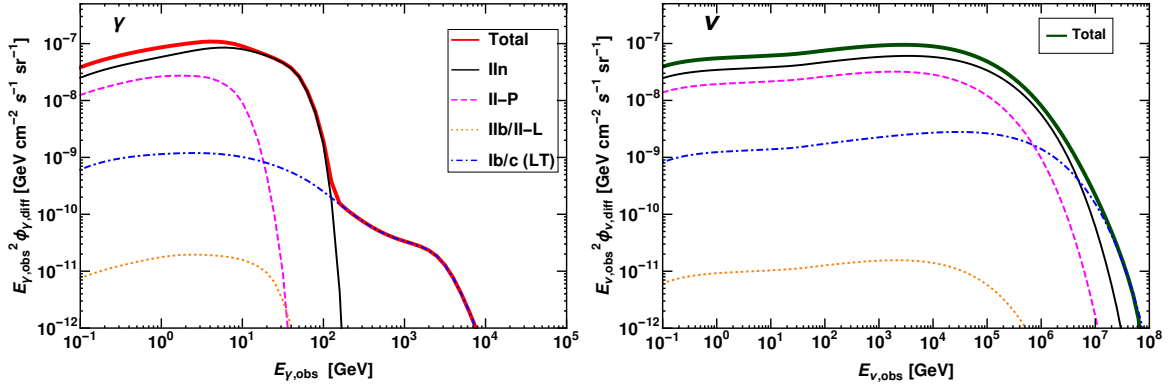


Figure 7. Diffuse gamma-rays (left) and all-flavour neutrinos (right) fluxes as functions of the observed particle energy for the different YSNe classes (see Table 1 for our benchmark model parameters). For both gamma-rays and neutrinos, Type IIIn (black solid curves) YSNe contribute the most to the total diffuse emission, followed by Type II-P (magenta dashed curves) YSNe at lower energies. The contribution (despite being small) from Type Ib/c (LT) (blue dot-dashed curves) YSNe may show up above 10^2 GeV in gamma-rays, whereas in neutrinos above 10^7 GeV. Type IIb/II-L (orange dotted curves) YSNe contribute negligibly. The flux of Type Ib/c YSNe is not shown since it lies outside the plot range. The total diffuse gamma-ray and neutrino fluxes are plotted as thick red and thick green curves. It can be seen that IIIn, II-P and Ib/c (LT) YSNe are the main contributors to the total diffuse spectra of both gamma-ray and neutrinos.

YSN Types by considering the benchmark values introduced in Table 1 and for $\alpha_p = 2.0$. The largest contribution to the diffuse emission comes from Type IIIn YSNe. The diffuse flux of Type II-P YSNe falls at around 20 GeV, i.e. at lower energies than Type IIIn YSNe because the thermal photons of Type II-P YSNe have larger average energies than the ones of Type IIIn YSNe ($\epsilon_{av} = 1$ eV for IIIn YSNe vs. $\epsilon_{av} = 4.6$ eV for II-P YSNe). The diffuse flux of Type Ib/c (LT) YSNe falls at larger observed gamma-ray energies than the one of Type IIIn YSNe because of the average energy of thermal photons. It has been found that Type II-P contributes small amount to the diffuse background at lower energies (below 10 GeV). Overall, the contribution of Type IIb/II-L, and Ib/c (LT) YSNe to the total diffuse gamma-ray background is negligible. However, a small diffuse flux of gamma-rays from Ib/c (LT) YSNe may show up above 10^2 GeV. Therefore, the total gamma-ray background (thick red curve) is mostly dominated by the contribution from Type IIIn SNe.

5.3 Diffuse background of high-energy neutrinos

The diffuse background of high-energy neutrinos for the different YSN Types can be computed by relying on Eq. 5.1. The crucial difference with respect to the diffuse gamma-ray flux is the loss of the gamma-ray flux due to the propagation.

The diffuse background of high-energy neutrinos is shown in the right panel of Fig. 7 for our benchmark model parameters introduced in Table 1 and for $\alpha_p = 2.0$. Similar to what observed for gamma-rays (see left panel of Fig. 7), the contribution from Type IIIn YSNe is larger than the one of Type II-P and Ib/c (LT) YSNe below $E_\nu = 10^7$ GeV. However, Type II-P YSNe also have significant contribution and their flux is smaller than IIIn YSNe by about a factor of 2. The diffuse flux of Type Ib/c (LT) is small at lower energies but might show up above $E_\nu = 10^7$ GeV, this is due to the fact that the maximum proton energy of this YSN Type is large because of the larger shock velocity and shock radius (see also Fig. 3). Also

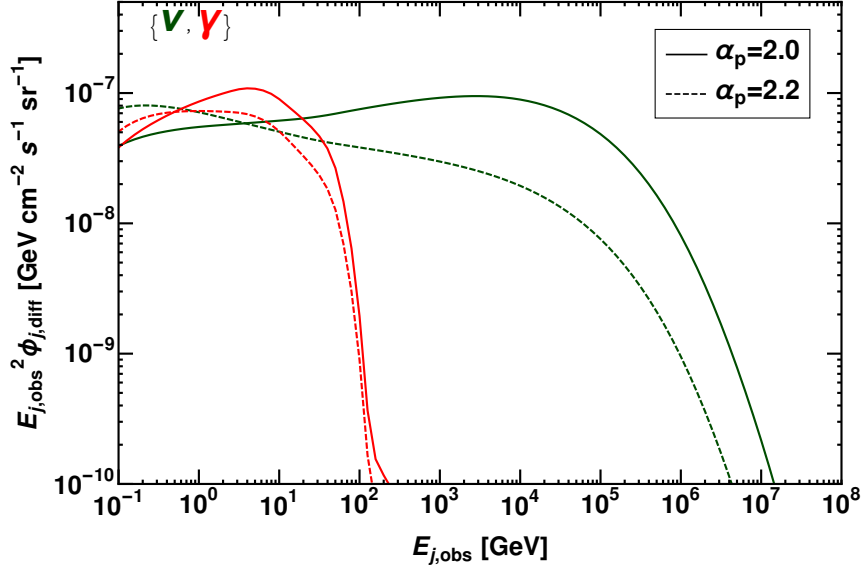


Figure 8. Diffuse backgrounds of gamma-rays (in red) and all-flavour neutrinos (dark green) for all YSNe Types as a function of the observed particle energy for $\alpha_p = 2.0$ (solid) and $\alpha_p = 2.2$ (dashed). The subscript j represents ν and γ . Larger values of α_p are responsible for softer energy spectra for both gamma-rays and neutrinos; the dependence of the diffuse spectrum on α_p is more pronounced for neutrinos than for gamma-rays.

note that the contribution of Type IIb/II-L YSNe to the total diffuse emission of high-energy neutrinos is negligible as the source flux of Type IIb/II-L YSNe is already quite small in comparison to the one of other Types of YSNe.

5.4 Model parameter uncertainties

The injection spectral index of protons crucially affects the high-energy diffuse backgrounds. Fig. 8 shows the total diffuse gamma-ray and neutrino backgrounds for $\alpha_p = 2.0$ (solid curves) and $\alpha_p = 2.2$ (dashed curves). Both diffuse backgrounds are larger for $\alpha_p = 2.0$ than that for $\alpha_p = 2.2$. This is due to the hardness of the energy distribution for $\alpha_p = 2.0$ at higher energies. Moreover, for gamma-rays, the EM cascaded flux of $\alpha_p = 2.0$ is larger than that obtained by using $\alpha_p = 2.2$. The dependence on α_p is more pronounced for neutrinos than for gamma-rays. This is because the higher energy part (above 100 GeV) of gamma-rays is heavily attenuated.

The left panel of Fig. 9 shows the total diffuse background of gamma-rays, including the contribution from all YSN Types. For reference, the diffuse background estimated for benchmark model parameters as in Table 1 and $\alpha_p = 2.0$ is represented by the solid red curve. The uncertainty band results from the convolution of the uncertainties on the parameters listed in Table 1. In particular, the model parameters mostly affecting the spectral distribution are v_{sh} , ϵ_p and ϵ_B ; the upper and lower limits of the parameters are reported in Table 2. Our choices on the upper limits for these model parameters are conservative compared to observations [67, 135, 136]. The remaining model parameters (see Table 1) are instead kept fixed. Note that we have not considered uncertainties on the benchmark parameters of Type IIb/II-L YSNe because their contribution to diffuse backgrounds is negligible. The lower limit of the gamma-ray diffuse emission is instead obtained for $\alpha_p = 2.2$ and shows a softer

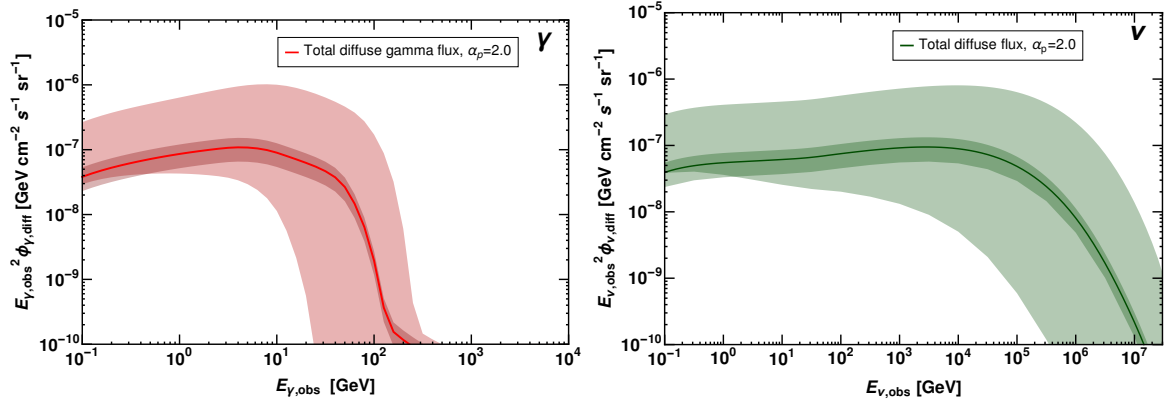


Figure 9. *Left panel:* Diffuse gamma-ray background from all Types of YSN as a function of the observed gamma-ray energy. The solid red line indicated our benchmark diffuse emission for $\alpha_p = 2.0$ and the other model parameters fixed as in Table 1. The band correspond to the uncertainties in shock velocity v_{sh} , power law α_p , fraction of kinetic energy ϵ_p and fraction of magnetic energy ϵ_B (see Table 2). The uncertainty associated to the local SN rate is represented by the thin band. *Right panel:* Correspondent diffuse all-flavour neutrino background. The uncertainty from model parameters is larger than the one from the SN rate.

Table 2. Uncertainties on a selection of model parameters of different YSN Types (see Table 1 for the benchmark parameters). Uncertainties on the model parameters of Type IIb/II-L and Ib/c YSN are not included because their contributions to diffuse backgrounds of high-energy particles is negligible.

Parameters	Type II _n		Type II-P		Type Ib/c (LT)	
	Upper	Lower	Upper	Lower	Upper	Lower
v_{sh} (kms ⁻¹)	9.5×10^3	5×10^3	2×10^4	8×10^3	2×10^4	5×10^3
ϵ_p	0.1	0.01	0.1	0.01	0.1	0.01
ϵ_B	10^{-2}	3×10^{-4}	3×10^{-2}	10^{-3}	3×10^{-2}	10^{-2}

energy distribution. In addition, the uncertainty associated to the local SN rate (see Sec. 5) might also have important consequences on the diffuse background spectra of gamma-rays and neutrinos. This uncertainty is included in our benchmark diffuse spectra and shown by the thin band. Interestingly, the uncertainty in the diffuse background from the SN rate is smaller than the one from the model parameters. Analogously, the right panel of Fig. 9 shows the total diffuse background of high-energy neutrinos.

5.5 Discussion

Fig. 10 summarizes our findings on the gamma-ray and neutrino diffuse emission from YSN. For reference, the data points of the Fermi-LAT Isotropic Gamma-ray Background (IGRB) between 100 MeV to 820 GeV are shown [171]. Moreover, the unexplained IGRB component in the range 50–1000 GeV is plotted with the purple dashed line [39, 172]. We also show the data points with error bars corresponding to 7.5 years by IceCube High-Energy Starting Event (HESE). The best fit to the IceCube data is represented by the black-dashed line; the related 68% confidence level uncertainty is plotted in cyan [3]. The diffuse neutrino flux sensitivity at 68% confidence level for KM3NeT is shown in light blue [173].

As for gamma-rays, a large fraction of the IGRB observed by Fermi-LAT may be coming

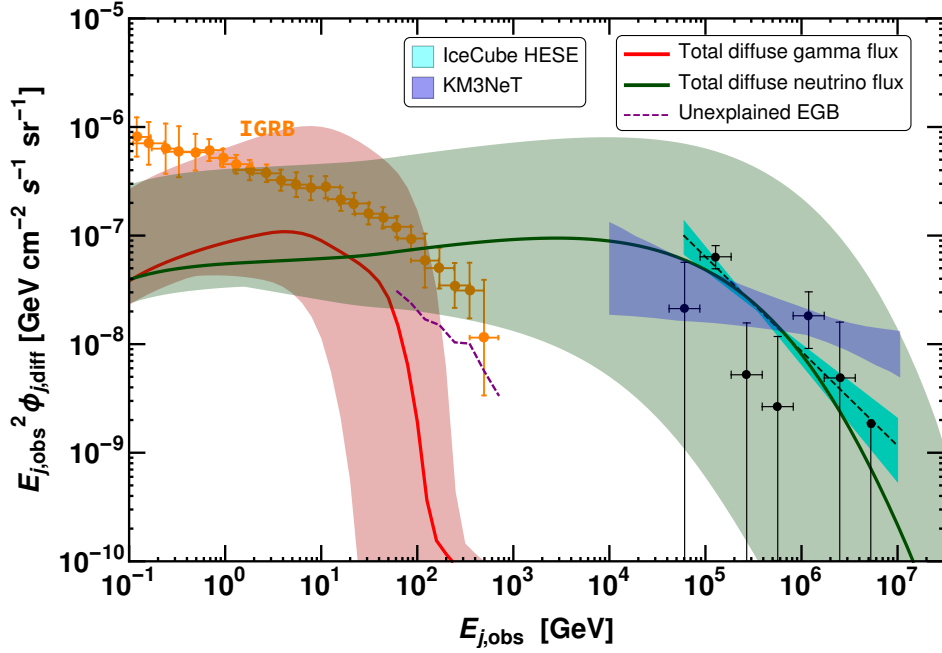


Figure 10. Total diffuse gamma-ray (in red) and all-flavour neutrino (in green) backgrounds from YSNe as functions of the observed particle energy, analogous to Fig. 9. The subscript j stands for ν or γ . For gamma-rays, the orange data points with error bars illustrate the diffuse gamma-ray background measured by Fermi-LAT (IGRB) [171]. The purple dashed curve shows the unexplained portion of the IGRB [47, 82, 172]. For neutrinos, the black-dashed line shows the IceCube (HESE) diffuse flux best fit for 7.5 years of data (black data points with error bars); the cyan band depicts the uncertainty on the IceCube diffuse flux at 68% confidence level [3]. The diffuse flux sensitivity of the future neutrino experiment KM3NeT is also shown by the light blue band [173]. It is evident that part of the parameter space considered for YSNe is ruled out from multi-messenger constraints from Fermi-LAT and IceCube. Nevertheless, our benchmark YSN parameters (Table 1) can very well explain part of the IceCube diffuse flux without the correspondent gamma-ray emission being in tension with the Fermi-LAT gamma-ray data. KM3NeT will further probe the diffuse neutrino flux from YSNe in the energy range 10^4 - 10^6 GeV.

from blazars, although recent work shows evidence for star-forming galaxies as the dominant contributors to the IGRB [52, 55, 59, 174, 175]. Our findings are in agreement with this picture on the IGRB composition. In fact, our benchmark YSN gamma-ray background (red solid line) is severely attenuated above 100 GeV and not in tension with blazar unexplained flux (purple dashed line). Moreover, the gamma-ray diffuse emission from star-forming galaxies should originate from the collisions of the SN accelerated protons with molecular clouds (ISM) in these active galaxies [176, 177] and therefore include the contribution of YSNe as well. However, the gamma-rays created in YSNe undergo larger attenuation (due to the dense CSM environment) than gamma-rays created in a thin ISM [59]. By comparing the diffuse gamma-ray emission predicted in this work with the Fermi-LAT data in Fig. 9, it is evident that our benchmark diffuse gamma flux is smaller than the Fermi-LAT IGRB and thus might negligibly contribute to the total SBG flux.

As for high-energy neutrinos, our benchmark YSN neutrino background is in good agreement with the IceCube HESE data below 10^6 GeV. Intriguingly, the YSN neutrino

background at low energies (10^4 – 10^5 GeV) is significantly large and can explain the HESE concentration at these energies, in alternative to dark sources or hypernovae [176, 178–181]. Within the YSN interpretation, the low-energy component of the neutrino diffuse background may originate from Type II_n SNe, whereas the neutrino diffuse background above 10^5 GeV may also have contributions from II-P and Ib/c (LT) SNe. This multi component interpretation, in addition to likely contributions to the neutrino diffuse emission from other sources, can accommodate possible different power laws in different energy ranges in future data fits of IceCube data [3]. The KM3NeT sensitivity shows that it will be able to probe the diffuse flux of neutrinos from YSNs in the energy range 10^4 – 10^6 GeV.

The contribution of YSNs may be subleading (e.g. for our benchmark model parameters) to the IGRB, however it could explain very well the observed IceCube diffuse emission below 10^6 GeV, relaxing the tension between gamma-ray and neutrino data for hadronic sources invoked as motivation for “hidden” sources [178]. Interestingly, part of the YSN parameter space allowed by multi-wavelength electromagnetic observations (see Table 2) may overshoot the Fermi-LAT and IceCube data, as shown by the bands in Fig. 10. This suggests that YSNs with such extreme model parameters are not representative of the YSN population.

The green and red solid curves in Fig. 10 have been obtained for $\epsilon_p = 0.01$ for Type II_n SNe. The maximum value allowed by the IGRB data is $\epsilon_p \simeq 0.03$, for which the corresponding neutrino background is enhanced by a factor of 3. Kinetic simulations predict ϵ_p as large as 0.2 [103], which may be in conflict with the high-energy diffuse backgrounds, if representative of the whole Type II_n YSN population.

The diffuse neutrino flux from Type II_n SNe reported in Ref. [19] relies on $\epsilon_p \sim 0.2$, which may be in tension with the Fermi-LAT IGRB. On the other hand, the Monte-Carlo simulations of Ref. [19] for randomly distributed ϵ_p in the range $[0.01, 0.1]$ produced a smaller diffuse flux, contributing up to 10% to the IceCube HESE flux. We find that the IceCube HESE data can be accommodated by smaller values of ϵ_p , thus remaining consistent with the IGRB data. In our case, the smaller ϵ_p is allowed as the total diffuse background also includes non-negligible contributions from Type II-P and Ib/c (LT) YSNs. In particular, Ib/c (LT) YSNs having the harder spectra dominate the higher energy tail above 1 PeV.

Our findings are also in agreement with the ones of Ref. [182], which estimated the neutrino and gamma-ray emission from a range of non-relativistic shock powered transients, concluding that the observed neutrino emission may come from gamma-ray dim sources. However, their model is based on optical observations of these transients, while we relied on YSN model parameters coming from a wide range of multi-wavelength surveys.

Upper limits on the high-energy diffuse neutrino background from SNe have been provided in Refs. [183, 184], which found that the diffuse neutrino background is dominated by SNe II-P, followed by SNe II_n and Ib/c. These findings are in contrast with ours because of the different choices of the local SN rates (Ref. [183] assumes $\xi = 52.4\%$ for SNe II-P, 6.4% for SNe II_n, and 25% for SNe Ib/c, while we considered the YSN fractions summarized in Fig. 5). In addition, Refs. [183, 184] do not take into account gamma-ray constraints.

We note that the larger mass loss rates of SNe II-P reported in Refs. [128, 129] (see also Sec. 3) can produce a diffuse emission from YSN II-P comparable to that of Type II_n SNe. This, in turn, may further constrain the parameters characteristics of the SN II_n population.

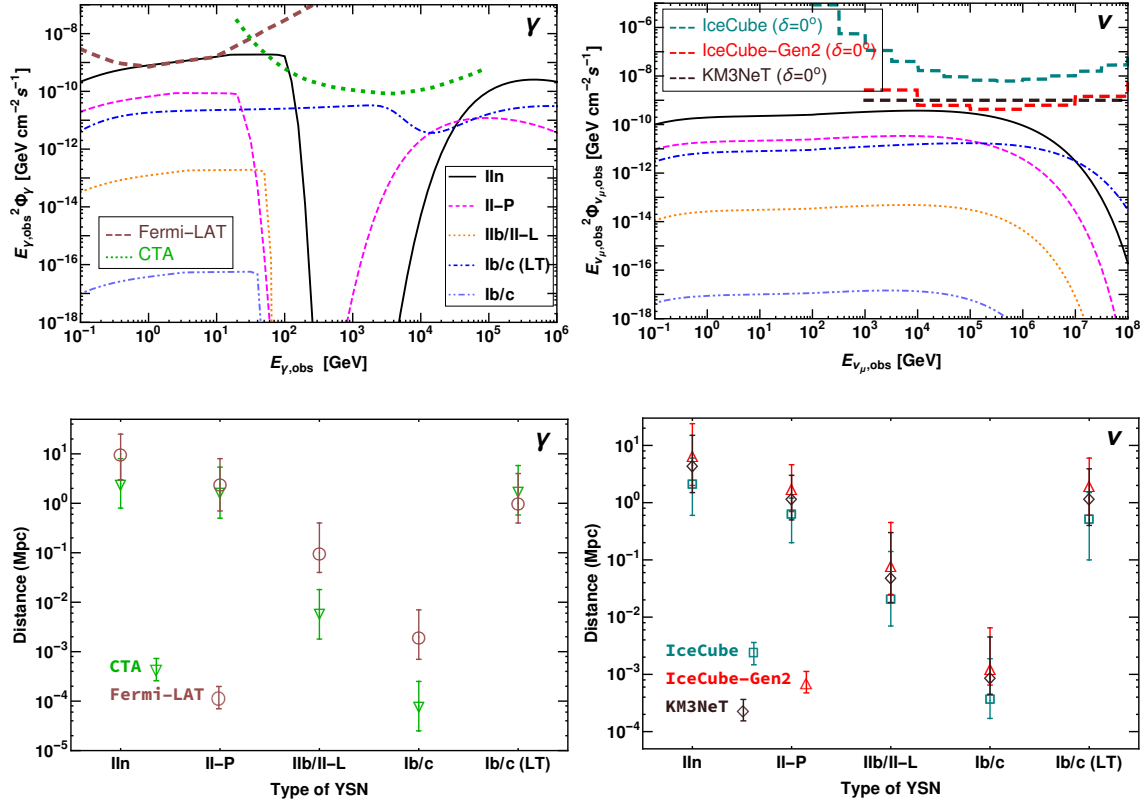


Figure 11. Detection prospects of nearby supernovae using gamma-ray (left) and neutrino telescopes (right). *Top left panel:* Gamma-ray energy fluxes from the different YSN Types at 10 Mpc as functions of the observed particle energy. The one year Fermi-LAT sensitivity is shown by the thick light brown dashed curve [85] and the thick green dotted curve represents the 100 hour CTA sensitivity [86]. Type IIn YSNs may be detected by both Fermi-LAT and CTA, while all other sources will be too dim at 10 Mpc. *Top right panel:* Corresponding muon neutrino energy fluxes. The sensitivities of IceCube, IceCube-Gen2 and KM3NeT for point source detection are plotted (thick dashed lines) in dark cyan (IceCube) [90], red (IceCube-Gen2) [91] and dark brown (KM3NeT) [92]. The sensitivities of IceCube, IceCube-Gen2 and KM3NeT are plotted for the declination angle $\delta = 0^\circ$. All these neutrino observatories will be able to detect YSNs at distances smaller than 10 Mpc. *Bottom left panel:* Gamma-ray YSN detection horizon for Fermi-LAT (light brown) and CTA (green) as functions of the YSN Type. For each YSN Type, the error band takes into account the model uncertainties (see Sec. 5.5). Fermi-LAT and CTA could detect YSNs up to 10 Mpc (see YSN IIn); CTA could have better sensitivity than Fermi-LAT and reach up to 2 Mpc for YSN Ib/c (LT). *Bottom right panel:* Corresponding neutrino YSN detection horizon for IceCube (dark cyan), IceCube-Gen2 (red) and KM3NeT (dark brown). IceCube-Gen2 will be able to detect YSNs up to ~ 4 Mpc (see YSN IIn).

6 Detection prospects of nearby young supernovae in gamma-rays and neutrinos

As shown in the previous Section, the diffuse backgrounds of neutrinos and gamma-rays from YSNs have large uncertainties due to the widely varying model parameters. The detection of neutrinos and gamma-rays from nearby YSNs will help to further constrain these model parameters and can potentially provide complementary understanding of shock-CSM inter-

actions. In the following, we investigate the detection prospects of YSNe with present and future gamma-ray telescopes and neutrino detectors.

Figure 11 illustrates the detection prospects for our benchmark YSNe in gamma-rays and neutrinos. The top panels display the energy flux expected at Earth for a YSN at 10 Mpc. The top left panel shows that the gamma-ray energy flux would be detectable for Type II_n YSN by Fermi-LAT [85] and CTA [86], while other SN Types can be probed at distances smaller than 10 Mpc. Interestingly, due to gamma-ray attenuation, dips could appear in the gamma-ray spectra between 100–1000 GeV (see related discussion for Fig. 2), CTA may be able to probe this feature for local YSNe. However, the detection of such dips requires more detailed analysis [185, 186]. The top right panel shows that corresponding neutrino flux from all YSNe are detectable in IceCube [90] below 10 Mpc, in agreement with Ref. [84]. Km3NeT [92] and IceCube-Gen2 [91] will also be able to detect neutrinos from these sources below 10 Mpc.

The bottom panels of Fig. 11 show the detection horizon of existing and upcoming gamma-ray and neutrino telescopes for the different YSN Types, by considering the model parameter uncertainties, see Table 2. The reach of different telescopes is calculated by taking into account the integrated flux of each YSN in the specific energy range of detectors’ best integral sensitivity. For gamma-rays, the energy range $[10^{-1}, 10^1]$ GeV is chosen for Fermi-LAT as it has the best integral sensitivity in this range. However, the whole energy range of CTA, i.e., $[2 \times 10^1, 7 \times 10^4]$ GeV is taken into account as the fluxes of most of YSNe are attenuated where CTA is most sensitive. The maximum reach of Fermi-LAT and CTA for different YSNe is shown in the bottom left panel of Fig. 11. Fermi-LAT and CTA could detect YSNe up to 10 Mpc (see YSNe II_n, for the benchmark parameters). However, Fermi-LAT has comparatively better sensitivity to YSNe than CTA except for Ib/c (LT) YSNe. This is due to the fact that CTA is more sensitive at higher energies and gamma-rays at these energies are attenuated by the thermal photons in the source. The exception of Ib/c (LT) YSNe is accounted for the small gamma-ray attenuation in the source (see top left plot and the discussion of Fig. 3). The detection horizon of CTA is affected by the amount of gamma-ray attenuation by the source thermal photons as discussed above. Thus, the detection of these sources in gamma-rays has the potential to unleash information about particle production, emission and propagation in YSNe.

Similarly, for the neutrino telescopes, we consider the YSNe fluxes in the energy range $[10^5, 10^6]$ GeV as these detectors have best sensitivity to the astrophysical neutrino flux in these energies (see the top right panel). The detection horizons marked in the plot refer to the ones for which the integrated flux is equal to the detectors’ integral sensitivity (see the top panels). For example, for YSNe Type II_n at distances above 2 Mpc, the integrated neutrino flux in the energy range 10^5 – 10^6 GeV would fall below the IceCube sensitivity at $\delta = 0^\circ$ declination. The error bars represent the uncertainties in the model parameters. Our findings concerning the detectability of neutrinos from YSNe II_n are in agreement with the ones of Ref. [19, 187]. Considering the uncertainties in the model parameters, IceCube-Gen2 will instead be able to detect Type II_n YSNe up to ~ 20 Mpc (4 Mpc for the benchmark parameters).

7 Conclusions

In this paper, we investigate the high energy neutrino and gamma ray signals from different classes of young SNe (Type II_n, II-P, IIb/II-L and Ib/c YSNe), up to one year after their

explosion. During this time, shock accelerated protons interact with the dense CSM around these objects, leading to the production of secondary high-energy neutrinos and gamma-rays. In particular, for the first time, we also investigate the late time emission of YSNe Ib/c, coming from the interaction of the SN shock with a dense hydrogen rich CSM far away from the stellar envelope.

Despite intense research activity, the origin of the bulk of the diffuse high-energy neutrino background observed by the IceCube Neutrino Observatory as well as the the Isotropic Gamma-Ray Background detected by Fermi-LAT is yet unknown. Our benchmark (intermediate) diffuse neutrino emission is in excellent agreement with the IceCube HESE data and suggests that YSNe could constitute the bulk of the high-energy diffuse neutrino emission observed by IceCube below 10^6 GeV, while being dim enough in gamma-rays to avoid any conflict with Fermi-LAT data.

The largest contribution to the diffuse neutrino emission mainly comes from Type II_n YSNe, followed by II-P and Ib/c (LT) YSNe, with Type II_n YSNe dominating the overall neutrino diffuse emission up to 10^7 GeV. Type Ib/c (LT) YSNe populate the diffuse neutrino emission above 10^7 GeV. The Type II-P YSN contribution is also significant, but smaller than the Type II_n SN one. Similar findings also hold for the diffuse gamma-ray background, after including all attenuation effects taking place both in the source and en route to Earth.

Intriguingly, the uncertainty bands obtained for the diffuse high-energy backgrounds by taking into account the uncertainties on the shock velocity, injection spectral index of protons, the kinetic and magnetic energy fractions, and the YSN rate suggest that a large fraction of the YSN parameter space inferred from multi-wavelength electromagnetic observations of YSNe is excluded by Fermi-LAT and IceCube HESE data.

The detection prospects of nearby YSNe with existing and upcoming gamma-ray and neutrino telescopes have also been explored. Among all YSNe, Type II_n SNe have the best discovery potential up to ~ 10 Mpc (~ 4 Mpc) in gamma-rays with Fermi-LAT and CTA (in neutrinos with IceCube, KM3NeT and IceCube-Gen2). Interestingly, CTA may be able to distinguish gamma-ray attenuation features in the spectral energy distributions for nearby transients. However, a possible amplification of magnetic field, e.g. due to Bell non-resonant streaming of cosmic rays, might influence proton acceleration and the gamma-ray spectra [see e.g., 188–190]. Multimessenger observations of such point sources will be able to probe these mechanisms and requires future dedicated work.

To conclude, the high-energy neutrino emission (especially coming from Type II_n, II-P and Ib/c (LT) SNe) can be a strong contender to explain the low-energy IceCube HESE dataset. The corresponding diffuse gamma ray emission is not in tension with the IGRB data from Fermi-LAT as YSNe gamma-rays are heavily attenuated and effectively “hidden.” The detection of high-energy particles from young supernovae will provide new insights on the processes linked to particle acceleration in young SNe.

Acknowledgments

We are grateful for helpful discussions with Madhurima Chakraborty, Jens Hjorth, Raffaella Margutti, and especially Tetyana Pitik. S.C acknowledges the support of the Max Planck India Mobility Grant from the Max Planck Society, supporting the visit and stay at MPP during the project. S.C has also received funding from DST/SERB projects CRG/2021/002961 and MTR/2021/000540. This project has received funding from the Villum Foundation (Project No. 37358), the Carlsberg Foundation (CF18-0183), the Deutsche Forschungsgemeinschaft

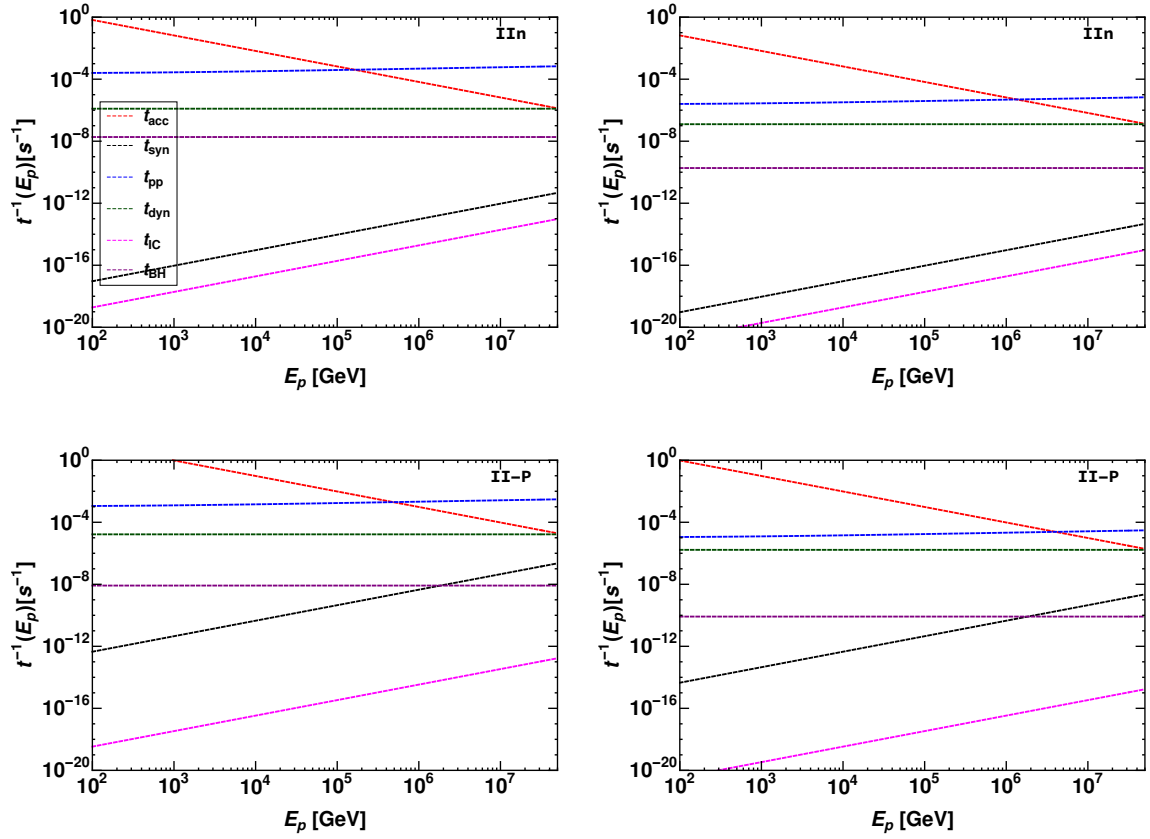


Figure 12. Acceleration time scale of protons and various proton energy loss processes as functions of the proton energy for Type IIIn YSNe (top panels) and Type II-P SNe (bottom panels) using the parameters in 1 and Sec. 4.2. The left panels show the interaction time for $r = r_{\text{in}}$, while right panels consider $r = 10 r_{\text{in}}$. Proton cooling is dominated by pp losses and therefore the total cooling timescale is the same as the pp collision timescale.

through Sonderforschungsbereich SFB 1258 “Neutrinos and Dark Matter in Astro- and Particle Physics” (NDM). Parts of this research were supported by the Australian Research Council Centre of Excellence for All Sky Astrophysics in 3 Dimensions (ASTRO 3D), through project number CE170100013.

A Characteristic timescales for proton acceleration and radiative processes

Shock accelerated protons lose energy through different processes such as pp interactions, dynamic or adiabatic losses, proton synchrotron, inverse Compton, Bethe-Heitler, etc. In this Appendix, we provide an overview of the different energy loss time scales for high energy protons and compare them with the acceleration time scales.

Acceleration time scale

The proton acceleration time scale is given by [104]:

$$t_{\text{acc}} = \frac{6E_p c}{eBv_{\text{sh}}^2}, \quad (\text{A.1})$$

where the magnetic field B is given in Sec. 2.1.

Adiabatic loss time scales

The adiabatic loss time scale for protons is same as the dynamical time scale and is given by:

$$t_{\text{ad}} \sim t_{\text{dyn}} = \frac{r}{v_{\text{sh}}}. \quad (\text{A.2})$$

Proton-proton collision time scale

The pp collision time scale is given by

$$t_{\text{pp}} = (\kappa_{\text{pp}} \sigma_{\text{pp}}(E_{\text{p}}) n_{\text{CSM}}(r) c)^{-1}, \quad (\text{A.3})$$

where $\kappa_{\text{pp}} = 0.5$ is the pp collision inelasticity.

Proton synchrotron time scale

High energy protons may lose energy due to proton synchrotron radiation. The corresponding synchrotron time scale is given by [191, 192]:

$$t_{\text{syn}} = \frac{\gamma m_{\text{p}} c^2}{P_{\text{syn}}}, \quad (\text{A.4})$$

where $\gamma = E_{\text{p}}/m_{\text{p}}c^2$ and P_{syn} is the synchrotron power loss and is given by

$$P_{\text{syn}} = \frac{4}{3} \sigma_{\text{T}} c \left(\frac{m_{\text{e}}}{m_{\text{p}}} \right)^2 \frac{B^2(r)}{8\pi} \left(\frac{v_{\text{sh}}}{c} \right)^2 \gamma^2, \quad (\text{A.5})$$

where σ_{T} is the Thomson scattering cross-section.

Inverse Compton loss time scales

Protons may lose energy to low energy SN photons via inverse Compton scattering and the corresponding loss time scale is given by [191]

$$t_{\text{IC}} = \frac{\gamma m_{\text{p}} c^2}{P_{\text{IC}}}, \quad (\text{A.6})$$

where the inverse Compton power P_{IC} is given by

$$P_{\text{IC}} = \frac{4}{3} \sigma_{\text{T}} c U_{\text{ph}}(r) \gamma^2 \left(\frac{v_{\text{sh}}}{c} \right)^2 \left(\frac{m_{\text{e}}}{m_{\text{p}}} \right)^2, \quad (\text{A.7})$$

where, $U_{\text{ph}}(r)$ is the energy density of photons in CSM [83]:

$$U_{\text{ph}}(r) = \frac{L_{\text{SN,pk}}}{(4\pi c r_{\text{in}}^2)} \left(\frac{r_{\text{in}}}{r} \right)^2. \quad (\text{A.8})$$

The SN peak luminosity $L_{\text{SN,pk}}$ for different YSNe can be found in Sec. 4.2.

Bethe-Heitler energy loss time scale

The Bethe-Heitler energy loss time scale is

$$t_{\text{BH}} = \tau_{\text{BH}} \left(\frac{r}{r_{\text{in}}} \right)^2 \quad (\text{A.9})$$

where $\tau_{\text{BH}}^{-1} = (\kappa_{\text{BH}} \sigma_{\text{BH}} c U_{\text{ph}}(r_{\text{in}})) / \epsilon_{\text{av}}$ and $\kappa_{\text{BH}} \sigma_{\text{BH}} \approx 6 \times 10^{-31} \text{ cm}^2$ [83].

Dominant energy loss processes

Fig. 12 shows the time scales introduced above as functions of the proton energy for the dominant YSN classes: SNe IIn (top panel) and II-P (bottom panel), see Table 1. Since the CSM density and SN thermal photon density change with the shock radius, the acceleration timescale and different cooling timescales also change. Therefore, we show the evolution of these timescales for two different values of shock radius, i.e., $r = r_{\text{in}}$ (left panel) and $r = 10r_{\text{in}}$ (right panel). For both classes of SNe, the dominant energy loss processes are pp collisions and adiabatic losses for both shock radii. Note that photo-hadronic ($p\gamma$) interactions are not important here as the average energy of SN thermal photons is about 1 eV; the threshold energy of protons for this process is ~ 10 PeV and the SN flux of protons above this energy is very small. Moreover, the cross-section of $p\gamma$ interactions ($\sim 10^{-28} \text{ cm}^2$ [45]) is much smaller than that of pp interaction ($\sim 10^{-26} \text{ cm}^2$ [44]).

References

- [1] ICECUBE collaboration, *Differential limit on the extremely-high-energy cosmic neutrino flux in the presence of astrophysical background from nine years of IceCube data*, *Phys. Rev. D* **98** (2018) 062003 [1807.01820].
- [2] ICECUBE collaboration, *IceCube Data for Neutrino Point-Source Searches Years 2008-2018*, [2101.09836](#).
- [3] ICECUBE collaboration, *The IceCube high-energy starting event sample: Description and flux characterization with 7.5 years of data*, *Phys. Rev. D* **104** (2021) 022002 [2011.03545].
- [4] ICECUBE collaboration, *Characteristics of the diffuse astrophysical electron and tau neutrino flux with six years of IceCube high energy cascade data*, *Phys. Rev. Lett.* **125** (2020) 121104 [2001.09520].
- [5] P. Meszaros, *Astrophysical Sources of High Energy Neutrinos in the IceCube Era*, *Ann. Rev. Nucl. Part. Sci.* **67** (2017) 45 [1708.03577].
- [6] M. Ahlers and F. Halzen, *Opening a New Window onto the Universe with IceCube*, *Prog. Part. Nucl. Phys.* **102** (2018) 73 [1805.11112].
- [7] E. Vitagliano, I. Tamborra and G. Raffelt, *Grand Unified Neutrino Spectrum at Earth: Sources and Spectral Components*, *Rev. Mod. Phys.* **92** (2020) 45006 [1910.11878].
- [8] N. Kurahashi, K. Murase and M. Santander, *High-Energy Extragalactic Neutrino Astrophysics*, [2203.11936](#).
- [9] P. Mészáros, *Gamma Ray Bursts as Neutrino Sources*, (2017), DOI [1511.01396].
- [10] T. Pitik, I. Tamborra and M. Petropoulou, *Neutrino signal dependence on gamma-ray burst emission mechanism*, *JCAP* **05** (2021) 034 [2102.02223].
- [11] K. Murase, *Active Galactic Nuclei as High-Energy Neutrino Sources*, in *Neutrino Astronomy: Current Status, Future Prospects*, T. Gaisser and A. Karle, eds., pp. 15–31 (2017), DOI [1511.01590].

- [12] E. Waxman, *The Origin of IceCube’s Neutrinos: Cosmic Ray Accelerators Embedded in Star Forming Calorimeters*, (2017), DOI [[1511.00815](#)].
- [13] I. Tamborra, S. Ando and K. Murase, *Star-forming galaxies as the origin of diffuse high-energy backgrounds: Gamma-ray and neutrino connections, and implications for starburst history*, *JCAP* **09** (2014) 043 [[1404.1189](#)].
- [14] F. Zandanel, I. Tamborra, S. Gabici and S. Ando, *High-energy gamma-ray and neutrino backgrounds from clusters of galaxies and radio constraints*, *Astron. Astrophys.* **578** (2015) A32 [[1410.8697](#)].
- [15] X.-Y. Wang and R.-Y. Liu, *Tidal disruption jets of supermassive black holes as hidden sources of cosmic rays: explaining the IceCube TeV-PeV neutrinos*, *Phys. Rev. D* **93** (2016) 083005 [[1512.08596](#)].
- [16] L. Dai and K. Fang, *Can tidal disruption events produce the IceCube neutrinos?*, *Mon. Not. Roy. Astron. Soc.* **469** (2017) 1354 [[1612.00011](#)].
- [17] N. Senno, K. Murase and P. Meszaros, *High-energy Neutrino Flares from X-Ray Bright and Dark Tidal Disruption Events*, *Astrophys. J.* **838** (2017) 3 [[1612.00918](#)].
- [18] C. Lunardini and W. Winter, *High Energy Neutrinos from the Tidal Disruption of Stars*, *Phys. Rev. D* **95** (2017) 123001 [[1612.03160](#)].
- [19] M. Petropoulou, S. Coenders, G. Vasilopoulos, A. Kamble and L. Sironi, *Point-source and diffuse high-energy neutrino emission from Type II supernovae*, *Mon. Not. Roy. Astron. Soc.* **470** (2017) 1881 [[1705.06752](#)].
- [20] I. Tamborra and S. Ando, *Inspecting the supernova–gamma-ray-burst connection with high-energy neutrinos*, *Phys. Rev. D* **93** (2016) 053010 [[1512.01559](#)].
- [21] P.B. Denton and I. Tamborra, *Exploring the Properties of Choked Gamma-ray Bursts with IceCube’s High-energy Neutrinos*, *Astrophys. J.* **855** (2018) 37 [[1711.00470](#)].
- [22] A. Palladino and W. Winter, *A multi-component model for observed astrophysical neutrinos*, *Astron. Astrophys.* **615** (2018) A168 [[1801.07277](#)].
- [23] I. Bartos, D. Veske, M. Kowalski, Z. Marka and S. Marka, *The IceCube Pie Chart: Relative Source Contributions to the Cosmic Neutrino Flux*, *Astrophys. J.* **921** (2021) 45 [[2105.03792](#)].
- [24] ICECUBE, FERMI-LAT, MAGIC, AGILE, ASAS-SN, HAWC, H.E.S.S., INTEGRAL, KANATA, KISO, KAPTEYN, LIVERPOOL TELESCOPE, SUBARU, SWIFT NUSTAR, VERITAS, VLA/17B-403 collaboration, *Multimessenger observations of a flaring blazar coincident with high-energy neutrino IceCube-170922A*, *Science* **361** (2018) eaat1378 [[1807.08816](#)].
- [25] P. Giommi, P. Padovani, F. Oikonomou, T. Glauch, S. Paiano and E. Resconi, *3HSP J095507.9+355101: a flaring extreme blazar coincident in space and time with IceCube-200107A*, *Astron. Astrophys.* **640** (2020) L4 [[2003.06405](#)].
- [26] A. Franckowiak et al., *Patterns in the Multiwavelength Behavior of Candidate Neutrino Blazars*, *Astrophys. J.* **893** (2020) 162 [[2001.10232](#)].
- [27] FERMI-LAT, ASAS-SN, ICECUBE collaboration, *Investigation of two Fermi-LAT gamma-ray blazars coincident with high-energy neutrinos detected by IceCube*, *Astrophys. J.* **880** (2019) 880:103 [[1901.10806](#)].
- [28] F. Krauß, K. Deoskar, C. Baxter, M. Kadler, M. Kreter, M. Langejahn et al., *Fermi/LAT counterparts of IceCube neutrinos above 100 TeV*, *Astron. Astrophys.* **620** (2018) A174 [[1810.08482](#)].
- [29] M. Kadler et al., *Coincidence of a high-fluence blazar outburst with a PeV-energy neutrino event*, *Nature Phys.* **12** (2016) 807 [[1602.02012](#)].

- [30] R. Stein et al., *A tidal disruption event coincident with a high-energy neutrino*, *Nature Astron.* **5** (2021) 510 [[2005.05340](#)].
- [31] S. Reusch et al., *The candidate tidal disruption event AT2019fdr coincident with a high-energy neutrino*, [2111.09390](#).
- [32] T. Pitik, I. Tamborra, C.R. Angus and K. Auchettl, *Is the High-energy Neutrino Event IceCube-200530A Associated with a Hydrogen-rich Superluminous Supernova?*, *Astrophys. J.* **929** (2022) 163 [[2110.06944](#)].
- [33] ICECUBE collaboration, *Follow-up of Astrophysical Transients in Real Time with the IceCube Neutrino Observatory*, *Astrophys. J.* **910** (2021) 4 [[2012.04577](#)].
- [34] VERITAS, MAGIC, ICECUBE, H.E.S.S., FACT collaboration, *Searching for VHE gamma-ray emission associated with IceCube neutrino alerts using FACT, H.E.S.S., MAGIC, and VERITAS*, *PoS ICRC2021* (2021) 960 [[2109.04350](#)].
- [35] A. Capanema, A. Esmaili and P.D. Serpico, *Where do IceCube neutrinos come from? Hints from the diffuse gamma-ray flux*, *JCAP* **02** (2021) 037 [[2007.07911](#)].
- [36] S. Ando, I. Tamborra and F. Zandanel, *Tomographic Constraints on High-Energy Neutrinos of Hadronuclear Origin*, *Phys. Rev. Lett.* **115** (2015) 221101 [[1509.02444](#)].
- [37] M.R. Feyereisen, I. Tamborra and S. Ando, *One-point fluctuation analysis of the high-energy neutrino sky*, *JCAP* **03** (2017) 057 [[1610.01607](#)].
- [38] E. Peretti, P. Blasi, F. Aharonian, G. Morlino and P. Cristofari, *Contribution of starburst nuclei to the diffuse gamma-ray and neutrino flux*, *Mon. Not. Roy. Astron. Soc.* **493** (2020) 5880 [[1911.06163](#)].
- [39] S. Chakraborty and I. Izaguirre, *Star-forming galaxies as the origin of IceCube neutrinos: Reconciliation with Fermi-LAT gamma rays*, [1607.03361](#).
- [40] D. Hooper, *A Case for Radio Galaxies as the Sources of IceCube’s Astrophysical Neutrino Flux*, *JCAP* **09** (2016) 002 [[1605.06504](#)].
- [41] T. Sudoh, T. Totani and N. Kawanaka, *High-energy gamma-ray and neutrino production in star-forming galaxies across cosmic time: Difficulties in explaining the IceCube data*, *Publ. Astron. Soc. Jap.* **70** (2018) 49 [[1801.09683](#)].
- [42] K. Murase, M. Ahlers and B.C. Lacki, *Testing the Hadronuclear Origin of PeV Neutrinos Observed with IceCube*, *Phys. Rev. D* **88** (2013) 121301 [[1306.3417](#)].
- [43] K. Wang, T.-Q. Huang and Z. Li, *Transient High-energy Gamma-rays and Neutrinos from Nearby Type II Supernovae*, *Astrophys. J.* **872** (2019) 157 [[1901.05598](#)].
- [44] S.R. Kelner, F.A. Aharonian and V.V. Bugayov, *Energy spectra of gamma-rays, electrons and neutrinos produced at proton-proton interactions in the very high energy regime*, *Phys. Rev. D* **74** (2006) 034018 [[astro-ph/0606058](#)].
- [45] S.R. Kelner and F.A. Aharonian, *Energy spectra of gamma-rays, electrons and neutrinos produced at interactions of relativistic protons with low energy radiation*, *Phys. Rev. D* **78** (2008) 034013 [[0803.0688](#)].
- [46] ICECUBE collaboration, *The IceCube high-energy starting event sample: Description and flux characterization with 7.5 years of data*, [2011.03545](#).
- [47] FERMI-LAT collaboration, *Resolving the Extragalactic γ -Ray Background above 50 GeV with the Fermi Large Area Telescope*, *Phys. Rev. Lett.* **116** (2016) 151105 [[1511.00693](#)].
- [48] C.D. Dermer, *The Extragalactic Gamma Ray Background*, *AIP Conf. Proc.* **921** (2007) 122 [[0704.2888](#)].
- [49] Y. Inoue, *Extragalactic Gamma-ray Background Radiation from Beamed and Unbeamed Active Galactic Nuclei*, *J. Phys. Conf. Ser.* **355** (2012) 012037 [[1108.1438](#)].

- [50] FERMI-LAT collaboration, *The Fermi-LAT high-latitude Survey: Source Count Distributions and the Origin of the Extragalactic Diffuse Background*, *Astrophys. J.* **720** (2010) 435 [[1003.0895](#)].
- [51] FERMI-LAT collaboration, *GeV Observations of Star-forming Galaxies with \textit{Fermi} LAT*, *Astrophys. J.* **755** (2012) 164 [[1206.1346](#)].
- [52] F.W. Stecker and T.M. Venters, *Components of the Extragalactic Gamma Ray Background*, *Astrophys. J.* **736** (2011) 40 [[1012.3678](#)].
- [53] M. Di Mauro, F. Donato, G. Lamanna, D.A. Sanchez and P.D. Serpico, *Diffuse γ -ray emission from unresolved BL Lac objects*, *Astrophys. J.* **786** (2014) 129 [[1311.5708](#)].
- [54] M. Ajello, M. Di Mauro, V.S. Paliya and S. Garrappa, *The γ -Ray Emission of Star-forming Galaxies*, *Astrophys. J.* **894** (2020) 88 [[2003.05493](#)].
- [55] M. Lisanti, S. Mishra-Sharma, L. Necib and B.R. Safdi, *Deciphering Contributions to the Extragalactic Gamma-Ray Background from 2 GeV to 2 TeV*, *Astrophys. J.* **832** (2016) 117 [[1606.04101](#)].
- [56] F. Massaro, D.J. Thompson and E.C. Ferrara, *The extragalactic gamma-ray sky in the Fermi era*, *Astron. Astrophys. Rev.* **24** (2016) 2 [[1510.07660](#)].
- [57] M. Fornasa and M.A. Sánchez-Conde, *The nature of the Diffuse Gamma-Ray Background*, *Phys. Rept.* **598** (2015) 1 [[1502.02866](#)].
- [58] K. Bechtol, M. Ahlers, M. Di Mauro, M. Ajello and J. Vandenbroucke, *Evidence against star-forming galaxies as the dominant source of IceCube neutrinos*, *Astrophys. J.* **836** (2017) 47 [[1511.00688](#)].
- [59] M.A. Roth, M.R. Krumholz, R.M. Crocker and S. Celli, *The diffuse γ -ray background is dominated by star-forming galaxies*, *Nature* **597** (2021) 341 [[2109.07598](#)].
- [60] F. Halzen and D. Hooper, *High-energy neutrino astronomy: The Cosmic ray connection*, *Rept. Prog. Phys.* **65** (2002) 1025 [[astro-ph/0204527](#)].
- [61] J.K. Becker, *High-energy neutrinos in the context of multimessenger physics*, *Phys. Rept.* **458** (2008) 173 [[0710.1557](#)].
- [62] K. Murase and I. Bartos, *High-Energy Multimessenger Transient Astrophysics*, *Ann. Rev. Nucl. Part. Sci.* **69** (2019) 477 [[1907.12506](#)].
- [63] I. Tamborra and K. Murase, *Neutrinos from Supernovae*, *Space Sci. Rev.* **214** (2018) 31.
- [64] R.A. Chevalier and C. Fransson, *Supernova interaction with a circumstellar medium*, *Lect. Notes Phys.* **598** (2003) 171 [[astro-ph/0110060](#)].
- [65] K. Murase, T.A. Thompson, B.C. Lacki and J.F. Beacom, *New Class of High-Energy Transients from Crashes of Supernova Ejecta with Massive Circumstellar Material Shells*, *Phys. Rev. D* **84** (2011) 043003 [[1012.2834](#)].
- [66] K. Murase, T.A. Thompson and E.O. Ofek, *Probing Cosmic-Ray Ion Acceleration with Radio-Submm and Gamma-Ray Emission from Interaction-Powered Supernovae*, *Mon. Not. Roy. Astron. Soc.* **440** (2014) 2528 [[1311.6778](#)].
- [67] N. Smith, *Mass Loss: Its Effect on the Evolution and Fate of High-Mass Stars*, *Ann. Rev. Astron. Astrophys.* **52** (2014) 487 [[1402.1237](#)].
- [68] N. Smith, *Circumstellar Material Around Evolved Massive Stars*, *Bulletin de la Societe Royale des Sciences de Liege* **80** (2011) 322 [[1010.3720](#)].
- [69] R. Margutti et al., *A panchromatic view of the restless SN2009ip reveals the explosive ejection of a massive star envelope*, *Astrophys. J.* **780** (2014) 21 [[1306.0038](#)].

- [70] R.M. Humphreys and K. Davidson, *The Luminous Blue Variables: Astrophysical Geysers*, *Publ. Astron. Soc. Pac.* **106** (1989) 1025.
- [71] N. Smith, *Luminous blue variables and the fates of very massive stars*, *Philosophical Transactions of the Royal Society A: Mathematical, Physical and Engineering Sciences* **375** (2017) 20160268.
- [72] K. Weis and D.J. Bomans, *Luminous Blue Variables*, *Galaxies* **8** (2020) 20 [2009.03144].
- [73] J.H. Groh, G. Meynet and S. Ekstrom, *Massive star evolution: Luminous Blue Variables as unexpected Supernova progenitors*, *Astron. Astrophys.* **550** (2013) L7 [1301.1519].
- [74] S. Ustamujic et al., *Modeling the remnants of core-collapse supernovae from luminous blue variable stars*, *Astron. Astrophys.* **654** (2021) A167 [2108.01951].
- [75] W. Jacobson-Galán et al., *Final Moments. I. Precursor Emission, Envelope Inflation, and Enhanced Mass Loss Preceding the Luminous Type II Supernova 2020tlf*, *Astrophys. J.* **924** (2022) 15 [2109.12136].
- [76] G. Terreran et al., *The Early Phases of Supernova 2020pni: Shock Ionization of the Nitrogen-enriched Circumstellar Material*, *Astrophys. J.* **926** (2022) 20 [2105.12296].
- [77] YOUNG SUPERNOVA EXPERIMENT collaboration, *An Early-time Optical and Ultraviolet Excess in the Type-Ic SN 2020oi*, *Astrophys. J.* **924** (2022) 55 [2105.09963].
- [78] E.O. Ofek et al., *SN 2010jl: Optical to Hard X-Ray Observations Reveal an Explosion Embedded in a Ten Solar Mass Cocoon*, *Astrophys. J.* **781** (2014) 42 [1307.2247].
- [79] P. Chandra, *Circumstellar interaction in supernovae in dense environments - an observational perspective*, *Space Sci. Rev.* **214** (2018) 27 [1712.07405].
- [80] S.J. Sturmer, J.G. Skibo, C.D. Dermer and J.R. Mattox, *Temporal evolution of nonthermal spectra from supernova remnants*, *Astrophys. J.* **490** (1997) 619.
- [81] P. Chandra, C.J. Stockdale, R.A. Chevalier, S.D. Van Dyk, A. Ray, M.T. Kelley et al., *Eleven years of radio monitoring of the Type II_n supernova SN 1995N*, *Astrophys. J.* **690** (2009) 1839 [0809.2810].
- [82] S. Chakraborty and I. Izaguirre, *Diffuse neutrinos from extragalactic supernova remnants: Dominating the 100 TeV IceCube flux*, *Phys. Lett. B* **745** (2015) 35 [1501.02615].
- [83] M. Petropoulou, A. Kamble and L. Sironi, *Radio synchrotron emission from secondary electrons in interaction-powered supernovae*, *Mon. Not. Roy. Astron. Soc.* **460** (2016) 44 [1603.00891].
- [84] K. Murase, *New Prospects for Detecting High-Energy Neutrinos from Nearby Supernovae*, *Phys. Rev. D* **97** (2018) 081301 [1705.04750].
- [85] Fermi-LAT, https://fermi.gsfc.nasa.gov/ssc/data/analysis/documentation/Cicerone/Cicerone_LAT_IRFs/LAT_sensitivity.html, .
- [86] M. Actis, G. Agnetta, F. Aharonian, A. Akhperjanian, J. Aleksić, E. Aliu et al., *Design concepts for the Cherenkov Telescope Array CTA: an advanced facility for ground-based high-energy gamma-ray astronomy*, *Experimental Astronomy* **32** (2011) 193 [1008.3703].
- [87] Q. Yuan, N.-H. Liao, Y.-L. Xin, Y. Li, Y.-Z. Fan, B. Zhang et al., *Fermi Large Area Telescope detection of gamma-ray emission from the direction of supernova iPTF14hls*, *Astrophys. J. Lett.* **854** (2018) L18 [1712.01043].
- [88] A. Gal-Yam, *Observational and Physical Classification of Supernovae*, in *Handbook of Supernovae*, A.W. Alsabti and P. Murdin, eds., p. 195 (2017), DOI.
- [89] M. Turatto, *Classification of supernovae*, *Lect. Notes Phys.* **598** (2003) 21 [astro-ph/0301107].

- [90] ICECUBE collaboration, *All-sky Search for Time-integrated Neutrino Emission from Astrophysical Sources with 7 yr of IceCube Data*, *Astrophys. J.* **835** (2017) 151 [[1609.04981](#)].
- [91] ICECUBE-GEN2 collaboration, *IceCube-Gen2: the window to the extreme Universe*, *J. Phys. G* **48** (2021) 060501 [[2008.04323](#)].
- [92] KM3NET collaboration, *Sensitivity of the KM3NeT/ARCA neutrino telescope to point-like neutrino sources*, *Astropart. Phys.* **111** (2019) 100 [[1810.08499](#)].
- [93] K. Murase, A. Franckowiak, K. Maeda, R. Margutti and J.F. Beacom, *High-Energy Emission from Interacting Supernovae: New Constraints on Cosmic-Ray Acceleration in Dense Circumstellar Environments*, *Astrophys. J.* **874** (2019) 80 [[1807.01460](#)].
- [94] F.W. Stecker, S.T. Scully and M.A. Malkan, *An Empirical Determination of the Intergalactic Background Light from UV to FIR Wavelengths Using FIR Deep Galaxy Surveys and the Gamma-ray Opacity of the Universe*, *Astrophys. J.* **827** (2016) 6 [[1605.01382](#)].
- [95] O.D. Fox et al., *On the Nature of Type Ia-CSM Supernovae: Optical and Near-Infrared Spectra of SN 2012ca and SN 2013dn*, *Mon. Not. Roy. Astron. Soc.* **447** (2015) 776 [[1408.6239](#)].
- [96] S.J. Sturmer, J.G. Skibo, C.D. Dermer and J.R. Mattox, *Temporal Evolution of Nonthermal Spectra from Supernova Remnants*, *Astrophys. J.* **490** (1997) 619.
- [97] A.R. Bell, *Particle acceleration by shocks in supernova remnants*, *Braz. J. Phys.* **44** (2014) 415 [[1311.5779](#)].
- [98] T.K. Gaisser, R. Engel and E. Resconi, *Cosmic Rays and Particle Physics*, Cambridge University Press, 2 ed. (2016), [10.1017/CBO9781139192194](#).
- [99] R.A. Chevalier, *Self-similar solutions for the interaction of stellar ejecta with an external medium.*, *Astrophys. J.* **258** (1982) 790.
- [100] A. Mastichiadis, *On the high-energy nonthermal emission from shell type supernova remnants*, *Astron. Astrophys.* **305** (1996) L53 [[astro-ph/9601132](#)].
- [101] E.O. Ofek et al., *Interaction-powered supernovae: Rise-time vs. peak-luminosity correlation and the shock-breakout velocity*, *Astrophys. J.* **788** (2014) 154 [[1404.4085](#)].
- [102] E. Waxman and B. Katz, *Shock breakout theory*, in *Handbook of Supernovae*, A.W. Alsabti and P. Murdin, eds., (Cham), pp. 967–1015, Springer International Publishing (2017), [DOI](#).
- [103] D. Caprioli and A. Spitkovsky, *Simulations of ion acceleration at non-relativistic shocks. i. acceleration efficiency*, *Astrophys. J.* **783** (2014) 91.
- [104] R.J. Protheroe and R.W. Clay, *Ultrahigh energy cosmic rays*, *Publ. Astron. Soc. Pac.* **21** (2004) 1 [[astro-ph/0311466](#)].
- [105] T. Piran, *The physics of gamma-ray bursts*, *Rev. Mod. Phys.* **76** (2005) 1143.
- [106] P. Meszaros, *Gamma-Ray Bursts*, *Rept. Prog. Phys.* **69** (2006) 2259 [[astro-ph/0605208](#)].
- [107] A. Marcowith, V. Dwarkadas, M. Renaud, V. Tatischeff and G. Giacinti, *Core collapse supernovae as Cosmic Ray sources*, *Mon. Not. Roy. Astron. Soc.* **479** (2018) 4470 [[1806.09700](#)].
- [108] A. Mastichiadis and J.G. Kirk, *Self-consistent particle acceleration in active galactic nuclei*, [astro-ph/9408077](#).
- [109] J.D. Finke and C.D. Dermer, *Cosmic-Ray Electron Evolution in the Supernova Remnant RX J1713.7-3946*, *Astrophys. J.* **751** (2012) 65 [[1203.4242](#)].
- [110] K. Murase, K. Kashiyama, K. Kiuchi and I. Bartos, *Gamma-Ray and Hard X-Ray Emission from Pulsar-Aided Supernovae as a Probe of Particle Acceleration in Embryonic Pulsar Wind Nebulae*, *Astrophys. J.* **805** (2015) 82 [[1411.0619](#)].

- [111] F.W. Stecker, M.A. Malkan and S.T. Scully, *Intergalactic photon spectra from the far ir to the uv lyman limit for $0 < Z < 6$ and the optical depth of the universe to high energy gamma-rays*, *Astrophys. J.* **648** (2006) 774 [[astro-ph/0510449](#)].
- [112] J.M. Jauch and F. Rohrlich, *The theory of photons and electrons. The relativistic quantum field theory of charged particles with spin one-half*, Texts and Monographs in Physics, Springer, Berlin, 2nd ed. ed. (1976), [10.1007/978-3-642-80951-4](#).
- [113] X.-C. Chang and X.-Y. Wang, *The diffuse gamma-ray flux associated with sub-PeV/PeV neutrinos from starburst galaxies*, *Astrophys. J.* **793** (2014) 131 [[1406.1099](#)].
- [114] L.A. Anchordoqui et al., *Cosmic Neutrino Pevatrons: A Brand New Pathway to Astronomy, Astrophysics, and Particle Physics*, *JHEAp* **1-2** (2014) 1 [[1312.6587](#)].
- [115] N. Smith et al., *Endurance of SN 2005ip after a decade: X-rays, radio and H α like SN 1988Z require long-lived pre-supernova mass-loss*, *Mon. Not. Roy. Astron. Soc.* **466** (2017) 3021 [[1612.02011](#)].
- [116] D. Pooley, J.C. Wheeler, J. Vinkó, V.V. Dwarkadas, T. Szalai, J.M. Silverman et al., *Interaction of SN 2004dk with a Previously-Expelled Envelope*, *Astrophys. J.* **833** (2019) 120 [[1910.06395](#)].
- [117] P. Chandra, R.A. Chevalier, N. Chugai, D. Milisavljevic and C. Fransson, *Supernova Interaction with a Dense Detached Shell in SN 2001em*, *Astrophys. J.* **902** (2020) 55 [[2008.13724](#)].
- [118] A. Balasubramanian, A. Corsi, E. Polisensky, T.E. Clarke and N.E. Kassim, *Radio Observations of SN2004dk with VLITE Confirm Late-time Rebrightening*, *Astrophys. J.* **923** (2021) 32 [[2101.07348](#)].
- [119] T. Szalai et al., *Spitzer's Last Look at Extragalactic Explosions: Long-term Evolution of Interacting Supernovae*, *Astrophys. J.* **919** (2021) 17 [[2106.12427](#)].
- [120] L. DeMarchi et al., *Radio Analysis of SN 2004C Reveals an Unusual CSM Density Profile as a Harbinger of Core Collapse*, [2203.07388](#).
- [121] T.J. Moriya, K. Maeda, F. Taddia, J. Sollerman, S.I. Blinnikov and E.I. Sorokina, *Mass-loss histories of Type II n supernova progenitors within decades before their explosion*, *Mon. Not. Roy. Astron. Soc.* **439** (2014) 2917 [[1401.4893](#)].
- [122] N. Smith, *Interacting Supernovae: Types II n and Ib n* , [1612.02006](#).
- [123] F. Taddia et al., *Carnegie Supernova Project: Observations of Type II n supernovae*, *Astron. Astrophys.* **555** (2013) A10 [[1304.3038](#)].
- [124] C.L. Ransome, S.M. Habergham-Mawson, M.J. Darnley, P.A. James, A.V. Filippenko and E.M. Schlegel, *A systematic reclassification of Type II n supernovae*, *Mon. Not. Roy. Astron. Soc.* **506** (2021) 4715 [[2107.02179](#)].
- [125] V.V. Dwarkadas, *On luminous blue variables as the progenitors of core-collapse supernovae, especially Type II n supernovae*, *Mon. Not. Roy. Astron. Soc.* **412** (2011) 1639 [[1011.3484](#)].
- [126] E.O. Ofek, L. Lin, C. Kouveliotou, G. Younes, E. Gogus, M.M. Kasliwal et al., *SN2009ip: Constraints on the progenitor mass-loss rate*, *Astrophys. J.* **768** (2013) 47 [[1303.3894](#)].
- [127] R.A. Chevalier and Z.-Y. Li, *Wind interaction models for gamma-ray burst afterglows: The Case for two types of progenitors*, *Astrophys. J.* **536** (2000) 195 [[astro-ph/9908272](#)].
- [128] V. Morozova, A.L. Piro and S. Valenti, *Unifying Type II Supernova Light Curves with Dense Circumstellar Material*, *Astrophys. J.* **838** (2017) 28 [[1610.08054](#)].
- [129] V. Morozova, A.L. Piro, M. Renzo and C.D. Ott, *Numerical Modeling of the Early Light Curves of Type IIP Supernovae*, *Astrophys. J.* **829** (2016) 109 [[1603.08530](#)].

- [130] S. Ekström, C. Georgy, P. Eggenberger, G. Meynet, N. Mowlavi, A. Wytenbach et al., *Grids of stellar models with rotation. I. Models from 0.8 to 120 M_{\odot} at solar metallicity ($Z = 0.014$)*, *aap* **537** (2012) A146 [[1110.5049](#)].
- [131] S.J. Smartt, *Observational constraints on the progenitors of core-collapse supernovae : the case for missing high mass stars*, *Publ. Astron. Soc. Austral.* **32** (2015) e016 [[1504.02635](#)].
- [132] A. Heger, C.L. Fryer, S.E. Woosley, N. Langer and D.H. Hartmann, *How massive single stars end their life*, *Astrophys. J.* **591** (2003) 288 [[astro-ph/0212469](#)].
- [133] G.A. Wagle and A. Ray, *Type IIP Supernova Progenitors. II. Stellar Mass and Obscuration by the Dust in the Circumstellar Medium*, *Astrophys. J.* **889** (2020) 86 [[1911.12831](#)].
- [134] T. Nakaoka et al., *The Low-luminosity Type IIP Supernova 2016bkv with Early-phase Circumstellar Interaction*, *Astrophys. J.* **859** (2018) 78 [[1804.06065](#)].
- [135] O. Yaron et al., *Confined Dense Circumstellar Material Surrounding a Regular Type II Supernova: The Unique Flash-Spectroscopy Event of SN 2013fs*, *Nature Phys.* **13** (2017) 510 [[1701.02596](#)].
- [136] C. Bullivant et al., *SN 2013fs and SN 2013fr: exploring the circumstellar-material diversity in Type II supernovae*, *Mon. Not. Roy. Astron. Soc.* **476** (2018) 1497 [[1801.01532](#)].
- [137] R. Margutti et al., *Ejection of the Massive Hydrogen-rich Envelope Time with the Collapse of the Stripped SN 2014C*, *Astrophys. J.* **835** (2017) 140 [[1601.06806](#)].
- [138] T.J. Moriya, F. Förster, S.-C. Yoon, G. Gräfener and S.I. Blinnikov, *Type IIP supernova light curves affected by the acceleration of red supergiant winds*, *Mon. Not. Roy. Astron. Soc.* **476** (2018) 2840 [[1802.07752](#)].
- [139] F. Förster et al., *The delay of shock breakout due to circumstellar material evident in most type II supernovae*, *Nature Astron.* **2** (2018) 808 [[1809.06379](#)].
- [140] N. Sravan, P. Marchant, V. Kalogera, D. Milisavljevic and R. Margutti, *Progenitors of Type IIb Supernovae: II. Observable Properties*, *Astrophys. J.* **903** (2020) 70 [[2009.06405](#)].
- [141] R. Ouchi and K. Maeda, *Radii and Mass-loss Rates of Type IIb Supernova Progenitors*, *Astrophys. J.* **840** (2017) 90 [[1705.02430](#)].
- [142] K.A. Bostroem et al., *Signatures of Circumstellar Interaction in the Type IIIc Supernova ASASSN-15oz*, *Mon. Not. Roy. Astron. Soc.* **485** (2019) 5120 [[1901.09962](#)].
- [143] S. Das and A. Ray, *Modeling type II-p/II-l supernovae interacting with recent episodic mass ejections from their presupernova stars with MESA and SNEC*, *Astrophys. J.* **851** (2017) 138.
- [144] T.M. Reynolds et al., *SN 2016gsd: An unusually luminous and linear type II supernova with high velocities*, *Mon. Not. Roy. Astron. Soc.* **493** (2020) 1761 [[1909.13617](#)].
- [145] A. Kamble, R. Margutti, A.M. Soderberg, S. Chakraborti, C. Fransson, R. Chevalier et al., *Radio and X-rays From SN 2013df Enlighten Progenitors of Type IIb Supernovae*, [1504.07988](#).
- [146] A. Gilkis and I. Arcavi, *How much hydrogen is in Type Ib and IIb supernova progenitors?*, *Mon. Not. Roy. Astron. Soc.* **511** (2022) 691 [[2111.04432](#)].
- [147] M.-K. Jung, S.-C. Yoon and H.-J. Kim, *Effects of Winds on the Optical Properties of Type Ib and Ic Supernova Progenitors*, *Astrophys. J.* **925** (2022) 216 [[2112.00272](#)].
- [148] D. Brethauer, R. Margutti, D. Milisavljevic and M. Bietenholz, *Six Years of Luminous X-Ray Emission from the Strongly Interacting Yype-Ib SN2014C Captured by Chandra and NuSTAR*, *Res. Notes AAS* **4** (2020) 235 [[2012.04081](#)].
- [149] S. Tinyanont et al., *Supernova 2014C: ongoing interaction with extended circumstellar material with silicate dust*, *Astrophys. J.* **887** (2019) 75 [[1909.06403](#)].

- [150] J.C. Mauerhan, W. Zheng, T. Brink, M.L. Graham, I. Shivvers, K. Clubb et al., *Stripped-envelope supernova SN 2004dk is now interacting with hydrogen-rich circumstellar material*, *Mon. Not. Roy. Astron. Soc.* **478** (2018) 5050 [1803.07051].
- [151] C.D. Kilpatrick et al., *A cool and inflated progenitor candidate for the Type Ib supernova 2019yvr at 2.6 yr before explosion*, *Mon. Not. Roy. Astron. Soc.* **504** (2021) 2073 [2101.03206].
- [152] F. Vargas, F. De Colle, D. Brethauer, R. Margutti and C.G. Bernal, *Survival of the Fittest: Numerical Modeling of SN 2014C*, *Astrophys. J.* **930** (2022) 150 [2102.12581].
- [153] D. Richardson, R.L. Jenkins, J. Wright and L. Maddox, *Absolute-Magnitude Distributions of Supernovae*, *Astron. J.* **147** (2014) 118 [1403.5755].
- [154] T.K. Gaisser, R.J. Protheroe and T. Stanev, *Gamma-ray production in supernova remnants*, *Astrophys. J.* **492** (1998) 219 [astro-ph/9609044].
- [155] A.A. Miller et al., *The Exceptionally Luminous Type II-L SN 2008es*, *Astrophys. J.* **690** (2009) 1303 [0808.2193].
- [156] S. Immler et al., *Swift and Chandra Detections of Supernova 2006jc: Evidence for Interaction of the Supernova Shock with a Circumstellar Shell*, *Astrophys. J. Lett.* **674** (2008) L85 [0712.3290].
- [157] M. Singh et al., *The fast evolving type Ib Supernova SN 2015dj in NGC 7371*, *Astrophys. J.* **909** (2021) 100 [2101.09430].
- [158] A. Kheirandish and K. Murase, *High-energy neutrinos from Supernovae: Prospects for Identification in Current and Future Neutrino Telescopes*, .
- [159] A. Kheirandish and K. Murase, *Detecting High-Energy Neutrino Minibursts from Local Supernovae with Multiple Neutrino Observatories*, **2204.08518**.
- [160] N. Smith, W. Li, A.V. Filippenko and R. Chornock, *Observed fractions of core-collapse supernova types and initial masses of their single and binary progenitor stars*, *Mon. Not. Roy. Astron. Soc.* **412** (2011) 1522 [1006.3899].
- [161] E. Cappellaro et al., *Supernova rates from the SUDARE VST-OmegaCAM search - I. Rates per unit volume*, *Astron. Astrophys.* **584** (2015) A62 [1509.04496].
- [162] PLANCK collaboration, *Planck 2015 results. XIII. Cosmological parameters*, *Astron. Astrophys.* **594** (2016) A13 [1502.01589].
- [163] L.-G. Strolger, T. Dahlen, S.A. Rodney, O. Graur, A.G. Riess, C. McCully et al., *The Rate of Core Collapse Supernovae to Redshift 2.5 From The CANDELS and CLASH Supernova Surveys*, *Astrophys. J.* **813** (2015) 93 [1509.06574].
- [164] J. Melinder, T. Dahlen, L. Mencía Trinchant, G. Östlin, S. Mattila, J. Sollerman et al., *The rate of supernovae at redshift 0.1-1.0. The Stockholm VIMOS Supernova Survey III*, *aap* **545** (2012) A96 [1206.6897].
- [165] P. Madau and M. Dickinson, *Cosmic Star Formation History*, *Ann. Rev. Astron. Astrophys.* **52** (2014) 415 [1403.0007].
- [166] E.E. Salpeter, *The Luminosity function and stellar evolution*, *Astrophys. J.* **121** (1955) 161.
- [167] H. Yuksel, M.D. Kistler, J.F. Beacom and A.M. Hopkins, *Revealing the High-Redshift Star Formation Rate with Gamma-Ray Bursts*, *Astrophys. J. Lett.* **683** (2008) L5 [0804.4008].
- [168] A. Lien, B.D. Fields and J.F. Beacom, *Synoptic Sky Surveys and the Diffuse Supernova Neutrino Background: Removing Astrophysical Uncertainties and Revealing Invisible Supernovae*, *Phys. Rev. D* **81** (2010) 083001 [1001.3678].
- [169] J.D. Finke, S. Razzaque and C.D. Dermer, *Modeling the Extragalactic Background Light from Stars and Dust*, *Astrophys. J.* **712** (2010) 238 [0905.1115].

- [170] A. Saldana-Lopez, A. Domínguez, P.G. Pérez-González, J. Finke, M. Ajello, J.R. Primack et al., *An observational determination of the evolving extragalactic background light from the multiwavelength HST/CANDELS survey in the Fermi and CTA era*, *Mon. Not. Roy. Astron. Soc.* **507** (2021) 5144 [[2012.03035](#)].
- [171] FERMI-LAT collaboration, *The spectrum of isotropic diffuse gamma-ray emission between 100 MeV and 820 GeV*, *Astrophys. J.* **799** (2015) 86 [[1410.3696](#)].
- [172] FERMI-LAT collaboration, *The spectrum of isotropic diffuse gamma-ray emission between 100 MeV and 820 GeV*, *Astrophys. J.* **799** (2015) 86 [[1410.3696](#)].
- [173] KM3NeT collaboration, *Sensitivity estimates for diffuse, point-like, and extended neutrino sources with KM3NeT/ARCA*, *JINST* **16** (2021) C09030 [[2107.13050](#)].
- [174] M. Di Mauro, S. Manconi, H.-S. Zechlin, M. Ajello, E. Charles and F. Donato, *Deriving the contribution of blazars to the Fermi-LAT Extragalactic γ -ray background at $E > 10$ GeV with efficiency corrections and photon statistics*, *Astrophys. J.* **856** (2018) 106 [[1711.03111](#)].
- [175] T. Linden, *Star-Forming Galaxies Significantly Contribute to the Isotropic Gamma-Ray Background*, *Phys. Rev. D* **96** (2017) 083001 [[1612.03175](#)].
- [176] N. Senno, P. Mészáros, K. Murase, P. Baerwald and M.J. Rees, *Extragalactic star-forming galaxies with hypernovae and supernovae as high-energy neutrino and gamma-ray sources: the case of the 10 TeV neutrino data*, *Astrophys. J.* **806** (2015) 24 [[1501.04934](#)].
- [177] H.J. Völk, F.A. Aharonian and D. Breitschwerdt, *The Nonthermal Energy Content and Gamma-Ray Emission of Starburst Galaxies and Clusters of Galaxies*, *Space Science Reviews* **75** (1996) 279.
- [178] K. Murase, D. Guetta and M. Ahlers, *Hidden Cosmic-Ray Accelerators as an Origin of TeV-PeV Cosmic Neutrinos*, *Phys. Rev. Lett.* **116** (2016) 071101 [[1509.00805](#)].
- [179] P.B. Denton and I. Tamborra, *The Bright and Choked Gamma-Ray Burst Contribution to the IceCube and ANTARES Low-Energy Excess*, *JCAP* **04** (2018) 058 [[1802.10098](#)].
- [180] M. Ahlers and F. Halzen, *Pinpointing Extragalactic Neutrino Sources in Light of Recent IceCube Observations*, *Phys. Rev. D* **90** (2014) 043005 [[1406.2160](#)].
- [181] K. Murase, S.S. Kimura and P. Meszaros, *Hidden Cores of Active Galactic Nuclei as the Origin of Medium-Energy Neutrinos: Critical Tests with the MeV Gamma-Ray Connection*, *Phys. Rev. Lett.* **125** (2020) 011101 [[1904.04226](#)].
- [182] K. Fang, B.D. Metzger, I. Vurm, E. Aydi and L. Chomiuk, *High-energy Neutrinos and Gamma Rays from Nonrelativistic Shock-powered Transients*, *Astrophys. J.* **904** (2020) 4 [[2007.15742](#)].
- [183] A. Stasik, *Search for High Energetic Neutrinos from Core Collapse Supernovae using the IceCube Neutrino Telescope*, Ph.D. thesis, 01, 2018.
- [184] ICECUBE collaboration, *Searching for High-Energy Neutrinos from Core-Collapse Supernovae with IceCube*, *PoS ICRC2021* (2021) 1116 [[2107.09317](#)].
- [185] P. Cristofari, A. Marcowith, M. Renaud, V.V. Dwarkadas, V. Tatischeff, G. Giacinti et al., *The first days of Type II-P core collapse supernovae in the gamma-ray range*, *Mon. Not. Roy. Astron. Soc.* **511** (2022) 3321 [[2201.09583](#)].
- [186] P. Cristofari, M. Renaud, A. Marcowith, V.V. Dwarkadas and V. Tatischeff, *Time-dependent high-energy gamma-ray signal from accelerated particles in core-collapse supernovae: the case of SN 1993J*, *Mon. Not. Roy. Astron. Soc.* **494** (2020) 2760 [[2004.02650](#)].
- [187] A. Marcowith, M. Renaud, V. Dwarkadas and V. Tatischeff, *Cosmic-ray acceleration and gamma-ray signals from radio supernovae*, *Nucl. Phys. B Proc. Suppl.* **256-257** (2014) 94 [[1409.3670](#)].

- [188] A.R. Bell, *Turbulent amplification of magnetic field and diffusive shock acceleration of cosmic rays*, *Mon. Not. Roy. Astron. Soc.* **353** (2004) 550.
- [189] V.N. Zirakashvili, V.S. Ptuskin and H.J. Volk, *Modeling Bell’s Non-resonant Cosmic Ray Instability*, *Astrophys. J.* **678** (2008) 255 [[0801.4486](#)].
- [190] C. Haggerty, D. Caprioli and E. Zweibel, *Hybrid Simulations of the Resonant and Non-Resonant Cosmic Ray Streaming Instability*, *PoS ICRC2019* (2020) 279 [[1909.06346](#)].
- [191] T. Padmanabhan, *Theoretical Astrophysics*, vol. 1, Cambridge University Press (2000), [10.1017/CBO9781139171083](#).
- [192] G. Ghisellini, G. Ghirlanda, G. Oganessian, S. Ascenzi, L. Nava, A. Celotti et al., *Proton–synchrotron as the radiation mechanism of the prompt emission of gamma-ray bursts?*, *Astron. Astrophys.* **636** (2020) A82 [[1912.02185](#)].